DRAFT VERSION JULY 13, 2015
Preprint typeset using LaTeX style emulateapj v. 5/2/11

arXiv:1410.6547v3 [astro-ph.SR] 10 Jul 2015

GRAND MINIMUM AND EQUATORWARD PROPAGATION IN A CYCLING STELLAR CONVECTIVE DYNAMO

KYLE AUGUSTSON[1], ALLAN SACHA BRUN[2], MARK MIESCH[1] & JURI TOOMRE[3]
[1]High Altitude Observatory, Center Green 1, Boulder, CO 80301, USA
[2]Laboratoire AIM Paris-Saclay, CEA/DSM – CNRS – Université Paris Diderot, IRFU/SAp, Gif-sur-Yvette, France and
[3]JILA and Dept. of Astrophysical & Planetary Sciences, University of Colorado, Boulder, CO 80309, USA
Draft version July 13, 2015

ABSTRACT

The 3-D magnetohydrodynamic (MHD) Anelastic Spherical Harmonic (ASH) code, using slope-limited diffusion, is employed to capture convective and dynamo processes achieved in a global-scale stellar convection simulation for a model solar-mass star rotating at three times the solar rate. The dynamo generated magnetic fields possesses many time scales, with a prominent polarity cycle occurring roughly every 6.2 years. The magnetic field forms large-scale toroidal wreaths, whose formation is tied to the low Rossby number of the convection in this simulation. The polarity reversals are linked to the weakened differential rotation and a resistive collapse of the large-scale magnetic field. An equatorial migration of the magnetic field is seen, which is due to the strong modulation of the differential rotation rather than a dynamo wave. A poleward migration of magnetic flux from the equator eventually leads to the reversal of the polarity of the high-latitude magnetic field. This simulation also enters an interval with reduced magnetic energy at low latitudes lasting roughly 16 years (about 2.5 polarity cycles), during which the polarity cycles are disrupted and after which the dynamo recovers its regular polarity cycles. An analysis of this grand minimum reveals that it likely arises through the interplay of symmetric and antisymmetric dynamo families. This intermittent dynamo state potentially results from the simulations relatively low magnetic Prandtl number. A mean-field-based analysis of this dynamo simulation demonstrates that it is of the α-Ω type. The time scales that appear to be relevant to the magnetic polarity reversal are also identified.

Subject headings: stars: magnetic field, rotation – convection – magnetohydrodynamics – turbulence

1. INTRODUCTION

The Sun exhibits many time scales, from the ten minute lifetimes of granules to multi-millennial magnetic activity modulations. One of the most prominent of these scales is the 11-year sunspot cycle, during which the number of magnetically active regions waxes and wanes. The Sun also possesses longer-term variability of its magnetic activity such as the 88-year Gleissberg cycle (Gleissberg 1939). There are also intermittent and aperiodic phenomenon commonly described as grand extrema (Usoskin 2013), such as the Maunder Minimum (Eddy 1976; Ribes & Nesme-Ribes 1993), wherein the overall magnetic activity of the Sun declines or increases for many polarity cycles relative to a long-term average. These longer-term trends in solar activity can be seen both in visual observations of the number of sunspots as well as in less direct measurements such as radioisotopic measurements (e.g., Beer et al. 1998). During grand minima, the number of sunspots tends to decrease and sometimes vanish for several polarity cycles. In contrast, their numbers increase over a grand maximum. Furthermore, during extrema such as the Maunder Minimum and the Modern Maximum, measurements of cosmogenic radioisotopes suggest that the heliospheric magnetic field strength can vary by at most a factor of five, but more typically by a factor of two (McCracken 2007). The simulation presented here shares some of these characteristics, where it shows disrupted cycles and a decrease in volume-averaged magnetic energy at lower latitudes during an extended interval covering several magnetic polarity cycles. So, the interval of disrupted magnetic cycles has been tagged as a "grand minimum."

In addition to its large range of time scales, the magnetic field at the solar surface exhibits complex, hierarchical structures that persist over a vast range of spatial scales. Nevertheless, large-scale organized spatial patterns of smaller structures such as Maunder's butterfly diagram, Joy's law, and Hale's polarity law suggest the existence of a structured large-scale magnetic field within the solar convection zone. On the Sun's surface active regions initially emerge at mid-latitudes and appear at progressively lower latitudes as the cycle progresses, thus exhibiting equatorward migration. In contrast, the diffuse field that is comprised of small-scale bipolar regions migrates toward the poles, with the global-scale reversal of the polar magnetic field occurring near solar maximum (e.g., Benevolenskaya 2004; Hathaway 2010).

Other main-sequence stars also exhibit observable magnetic phenomenon under several measures such as Ca II, photometric, spectropolarimetric, and X-ray observations (e.g., Baliunas et al. 1996; Hempelmann et al. 1996; Favata et al. 2008; Metcalfe et al. 2010; Fares et al. 2013; Mathur et al. 2013). Such observations have shown that solar-mass stars younger than the Sun can also possess magnetic activity cycles. These younger stars tend to rotate more rapidly than the Sun as a consequence of having been born with a relatively high angular momentum and due to their relatively slow rate of angular momentum loss (e.g., Barnes 2007; Matt et al. 2015). There are further hints from both observations and from theory that stellar magnetic cycle periods should be linked to its rotation rate (e.g., Saar 2009; Jouve et al. 2010; Morgenthaler et al. 2011). So, in some senses, the simulation presented here could be considered to be capturing some of the dynamo behavior of a young Sun-like star. Moreover, from a theoretical point of view, the ratio of the polarity cycle period to the relevant dynamical time scales of the rotation period may be of more interest. For the Sun, this ratio is about 287, and as will be seen later this ratio is about 243 for this model.

1.1. *Cyclic Convective Dynamo Action*

It has been suspected for at least 60 years that the crucial ingredients for the solar dynamo are the shear of the differential rotation and the helical nature of the small-scale convective flows present in the solar convection zone (e.g., Parker 1955; Steenbeck & Krause 1969; Parker 1977). Though other models and observations suggest that the surface magnetic fields play a significant role, such as in the Babcock-Leighton dynamo mechanism (e.g., Babcock 1961; Charbonneau et al. 2005; Miesch & Brown 2012). Such models have been fairly successful in capturing aspects of the solar cycles. However, when adopting fully nonlinear global-scale 3-D MHD simulations (e.g., Gilman 1983; Glatzmaier 1985; Brun et al. 2004; Browning et al. 2006), it has been challenging to achieve dynamo action that exhibits a majority of the properties of Sun's large-scale magnetism.

Recent global-scale simulations of convective dynamos have begun to make substantial contact with some of the properties of the solar dynamo using a wide variety of numerical methods (e.g., Ghizaru et al. 2010; Brown et al. 2011; Racine et al. 2011; Käpylä et al. 2012; Augustson et al. 2013; Passos & Charbonneau 2014; Fan & Fang 2014). The simulation analyzed here fits within this vein of modern stellar dynamo modeling, where it exhibits some features akin to those observed during solar and stellar cycles. In particular, global-scale convective dynamo simulations in rotating spherical shells have recently achieved the long-sought goal of cyclic magnetic polarity reversals with a multi-decadal period. Moreover, some of these simulations have illustrated that large-scale dynamo action is possible within the bulk of the convection zone, even in the absence of a tachocline (e.g., Brun et al. 2004; Brown et al. 2010; Käpylä et al. 2012).

Global-scale MHD simulations of a more rapidly rotating Sun with the ASH code have produced polarity-reversing dynamo action that possesses strong toroidal wreaths of magnetism that propagate poleward as a cycle progresses (Brown et al. 2011). These fields are contained within the convection zone itself, with the majority of the magnetic energy present near the lower boundary. Furthermore, a recent simulation with ASH employs a dynamic Smagorinski diffusion scheme, wherefore a greater level of turbulent complexity is achieved for the resolved spatial structures. Those simulations show that the large-scale toroidal wreaths persist despite the greater pummeling they endure from the more complex and vigorous convection (Nelson et al. 2013a). Not only do the toroids of field persevere, but portions of them can be so amplified that the combination of upward advection and magnetic buoyancy create loops of magnetic field that rise upward toward the surface (Nelson et al. 2013b).

1.2. *Differing Approaches to Sub-Grid-Scale Dissipation*

Both explicit and implicit large-eddy simulations (LES and ILES) have concurrently paved the road toward more orderly long-term cycles in a setting that may mimic the solar interior. Indeed, the first 3-D simulation to produce regular polarity cycles over a long time period utilized the Eulerian-Lagrangian magnetohydrodynamics code (EULAG-MHD) (Ghizaru et al. 2010). The polarity cycles in that simulation occur roughly every 80 years, with the magnetic fields existing primarily at higher latitudes and within the tachocline at the base of the convection zone (e.g., Racine et al. 2011; Passos & Charbonneau 2014). Such dynamo action is likely made possible through two mechanisms: the first being that the ILES formulation of EULAG attempts to maximize the complexity of the flows and magnetic fields for a given Eulerian grid resolution, and the second being the reduction of the enthalpy transport of the largest scales through a relatively simple sub-grid-scale (SGS) model. The latter mechanism operates through the dissipation of entropy structures by adding a thermal drag to the entropy equation. This reduces the buoyancy of the resolved convective structures, and thereby the root-mean-square velocities, which in turn decreases the Rossby number.

The magnetic fields in those EULAG-MHD simulations, however, have primarily shown radial propagation of structures but little latitudinal variation during a cycle. Though much like prior simulations using ASH, a recent EULAG-MHD simulation of a Sun-like star rotating at thrice the solar rate can also produce low-latitude poleward propagating solutions (Charbonneau 2013). Similarly, 3-D MHD simulations in spherical segments employing the Pencil code also possess regularly cyclic magnetic polarity reversals in addition to a rich set of other behavior. In particular, a few of those polarity reversing solutions were the first to exhibit low-latitude equatorward propagating magnetic features (Käpylä et al. 2011a, 2013). In those simulations, the stratification and a sufficient level of turbulence appear to be necessary to achieve the phase alignment between the magnetic field and the differential rotation required to produce the dynamo wave phenomenon known as the Parker-Yoshimura effect (Warnecke et al. 2014).

Inspired by those recent results, a slope-limited diffusion (SLD) scheme was incorporated into ASH with the express goal of achieving a low effective Pr and Pm dynamo, thus attempting to better mimic the low fluid and magnetic Prandtl numbers present in the solar interior. This effort minimizes the effects of viscosity, and so extends the inertial range as far as possible for a given resolution, whereas the thermal and magnetic fields retain their LES-SGS eddy diffusivities. Consequently, SLD permits more scales to be captured before entering the dissipation range. This in turn allows more scale separation between the larger magnetic and and smaller kinetic scales participating in the low Pm dynamo (Ponty et al. 2005; Schekochihin et al. 2007; Brandenburg 2009), given that the ratio of the magnetic to the viscous dissipation scales is greater than unity. Subsequently, the kinetic helicity is also greater at small scales than otherwise would be achieved with the required Newtonian momentum diffusion at the same resolution, which has been shown to have a large influence on the dynamo efficiency (Malyshkin & Boldyrev 2010).

With the newly implemented SLD scheme, a solution has been found that possesses features similar to those of the solar dynamo: (i) a regular magnetic polarity cycle, though with a period of 6.2 years, in which the magnetic polarity reversals occur near the maximum in the magnetic energy, (ii) an equatorward propagation of magnetic features, (iii) a poleward migration of oppositely-signed flux, and (iv) the equilibrium of regular cycles is punctuated by an interval where the cycling behavior is disrupted, the magnetic energy is reduced at low latitudes, and after which the cycle is recovered. In keeping with the ASH nomenclature for related cases as in Brown et al. (2010, 2011) and Nelson et al. (2013a), this dynamo solution has been called case K3S.

1.3. *General Layout*

The basic layout of the paper is as follows: §2 contains the details of the equations solved and of their numerical implementation; §3 provides an overview of the dynamics of the

solution and references to each of the relevant in-depth analysis sections. Then §4 assesses the properties of the typical polarity cycles and the mechanisms contributing to the evolution of the poloidal magnetic field within this dynamo. The grand minimum seen in this simulation and its properties are discussed in §5. The processes relevant to the equatorward propagation of the magnetic fields during a cycle are covered in §6. An analysis of time scales is given in §7. Connections to a mean-field description of the simulation are made in §8. Discussion of the significance of our findings with K3S, and their relation to other studies, is provided in the concluding §9. Appendix A defines the operators used in slope-limited diffusion and illustrates some of its properties. Appendix B provides a derivation of equations governing the evolution of the kinetic energy contained in the differential rotation.

2. COMPUTATIONAL METHODS

The 3-D simulation of convective dynamo action presented here as case K3S uses the ASH code to evolve the Lantz-Braginski-Roberts (LBR) form of the anelastic MHD equations for a conductive plasma in a rotating spherical shell. ASH solves those equations employing a pseudo-spectral method with spherical harmonic expansions in the horizontal directions of the entropy, magnetic field, pressure, and mass flux (Clune et al. 1999; Miesch et al. 2000). A fourth-order non-uniform finite difference in the radial direction resolves the radial derivatives. The solenoidality of the mass flux and magnetic vector fields is maintained through the use of a streamfunction formalism (Brun et al. 2004). The density, entropy, pressure, and temperature are linearized about the spherically symmetric background values $\overline{\rho}$, $\overline{S}$, $\overline{P}$, and $\overline{T}$ respectively, which are functions of the radial coordinate only. These linearized thermodynamic variables are denoted ρ, S, P, and T. The reduced pressure $\varpi = P/\overline{\rho}$ is used in the LBR implementation from which the equivalent thermodynamic pressure fluctuations can be recovered. The equations solved in ASH retain physical units, are in spherical coordinates (r,θ,φ), and are evolved in time t as

$$\text{continuity:} \quad \boldsymbol{\nabla}\cdot\overline{\rho}\mathbf{v} = 0, \tag{1}$$

$$\text{momentum:} \quad \overline{\rho}\frac{\partial \mathbf{v}}{\partial t} = -\overline{\rho}\mathbf{v}\cdot\boldsymbol{\nabla}\mathbf{v} - \boldsymbol{\nabla}\varpi + \frac{Sg}{c_P}\hat{\mathbf{r}} + 2\overline{\rho}\mathbf{v}\times\hat{\boldsymbol{\Omega}}_0 + \frac{1}{4\pi}(\boldsymbol{\nabla}\times\mathbf{B})\times\mathbf{B} + \boldsymbol{\nabla}\cdot\mathcal{D}, \tag{2}$$

$$\text{energy:} \quad \overline{\rho}\overline{T}\frac{\partial S}{\partial t} = -\overline{\rho}\overline{T}\mathbf{v}\cdot\boldsymbol{\nabla}\left(\overline{S}+S\right) - \nabla\cdot\mathbf{q} + \Phi, \tag{3}$$

$$\text{flux conservation:} \quad \boldsymbol{\nabla}\cdot\mathbf{B} = 0, \tag{4}$$

$$\text{induction:} \quad \frac{\partial \mathbf{B}}{\partial t} = \boldsymbol{\nabla}\times[\mathbf{v}\times\mathbf{B} - \eta\boldsymbol{\nabla}\times\mathbf{B}], \tag{5}$$

with the velocity field being $\mathbf{v} = \mathrm{v_r}\hat{\mathbf{r}} + \mathrm{v}_\theta\hat{\boldsymbol{\theta}} + \mathrm{v}_\varphi\hat{\boldsymbol{\varphi}}$, and the magnetic field being $\mathbf{B} = B_\mathrm{r}\hat{\mathbf{r}} + B_\theta\hat{\boldsymbol{\theta}} + B_\varphi\hat{\boldsymbol{\varphi}}$. $\hat{\boldsymbol{\Omega}}_0 = \Omega_0\hat{\mathbf{z}}$ is the angular velocity of the rotating frame, $\hat{\mathbf{z}}$ is the direction along the rotation axis, and the magnitude of the gravitational acceleration is g. The diffusion tensor $\mathcal{D}$, which includes both viscous and slope-limited components, and the dissipative term Φ are

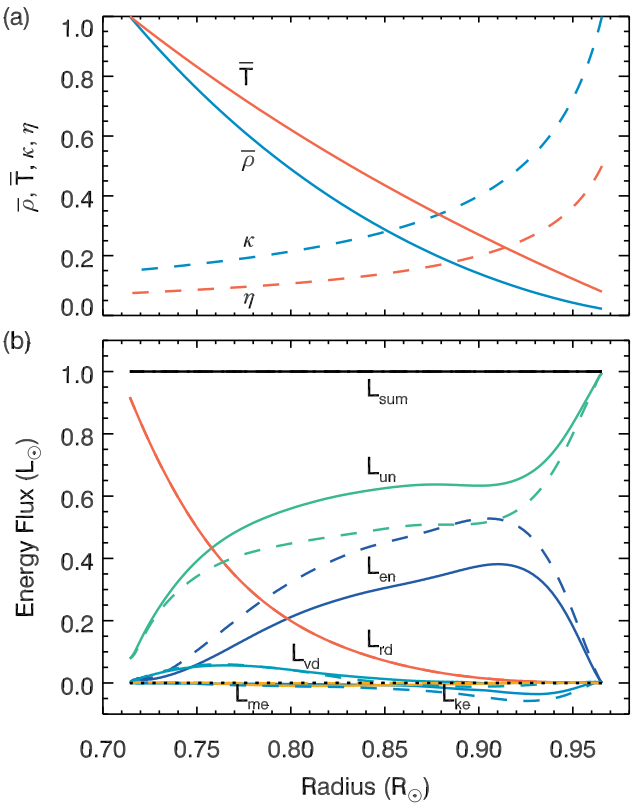

Figure 1. Background stratification and energy flux balance in K3S as a function of fractional solar radius ($r/\mathrm{R}_\odot$). (a) The isentropic background state, showing $\overline{\rho}$ (solid blue) and $\overline{T}$ (solid red). The entropy diffusion coefficient κ and magnetic diffusion coefficient η are shown as the dashed-blue and dashed-red lines respectively. All quantities have been normalized by their maximum value. (b) The time and horizontally-averaged radial energy fluxes represented as luminosities (e.g., the flux in a quantity x is $L_x = 4\pi r^2 F_x$) in units of the solar luminosity ($L_\odot = 3.86\times10^{33}$ erg s^{-1}). The fluxes are shown averaged over two intervals, with solid lines averaged around a magnetic energy maximum and the dashed lines near a magnetic energy minimum. The lines are total flux (L_{sum}) in black, radiative flux (L_{rd}) in red, enthalpy flux (L_{en}) in blue, conductive entropy flux (L_{un}) in green, kinetic energy (L_{ke}) in light blue, slope-limited diffusion flux (L_{vd}) in teal, and Poynting flux in (L_{me}) orange.

$$\mathcal{D}_{ij} = 2\overline{\rho}\nu\left[e_{ij} - \frac{1}{3}\boldsymbol{\nabla}\cdot\mathbf{v}\delta_{ij}\right] + \mathcal{F}^{\mathrm{sld}}_{\mathbf{v},ij}, \tag{6}$$

$$\Phi = 2\overline{\rho}\nu\left[e_{ij}e_{ij} - \frac{1}{3}(\boldsymbol{\nabla}\cdot\mathbf{v})^2\right] + \frac{4\pi\eta}{c^2}\mathbf{J}^2 + \boldsymbol{\nabla}\cdot\mathbf{F}^{\mathrm{sld}}_{\mathrm{ke}} - \overline{\rho}\mathbf{v}\cdot\boldsymbol{\nabla}\cdot\mathcal{F}^{\mathrm{sld}}_{\mathbf{v}}, \tag{7}$$

involving the stress tensor e_{ij}, the effective kinematic eddy viscosity ν, the magnetic eddy resistivity η, and the current density $\mathbf{J} = c/4\pi\boldsymbol{\nabla}\times\mathbf{B}$. The slope-limited velocity diffusion tensor is $\mathcal{F}^{\mathrm{sld}}_{\mathbf{v}}$, the kinetic energy slope-limited diffusion flux vector is $\mathbf{F}^{\mathrm{sld}}_{\mathrm{ke}}$, and they are computed using the algorithm shown in Appendix A. The difference of the divergence of the two fluxes accounts for the change in entropy due to the SLD operator acting on the velocity field. The energy flux $\mathbf{q}$ is comprised of a radiation flux (in the diffusion approximation) and an inhomogeneous turbulent entropy diffusion flux,

$$\mathbf{q} = \kappa_r\overline{\rho}c_\mathrm{P}\boldsymbol{\nabla}\left(\overline{T}+T\right) + \kappa\overline{\rho}\overline{T}\boldsymbol{\nabla}S, \tag{8}$$

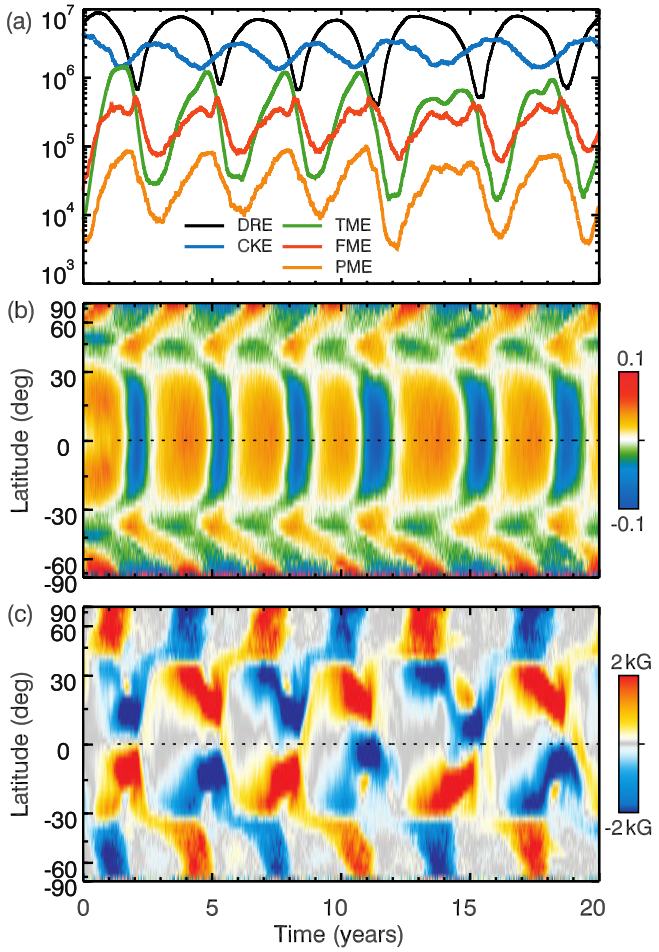

Figure 2. Evolution of the energy densities as well as the angular velocity variations and mean (longitudinally-averaged) toroidal magnetic field $\langle B_\varphi \rangle$ at $0.92\,\mathrm{R}_\odot$ over the first 20 years of the simulation. (a) Time variation of the volume-averaged energy density of the differential rotation (DRE, black), nonaxisymmetric flows (CKE, blue), axisymmetric toroidal magnetic energy (TME, green), axisymmetric poloidal magnetic energy (PME, orange), and nonaxisymmetric magnetic energy (FME, red) in units of $\mathrm{erg\,cm^{-3}}$ (b) Time-latitude diagram of angular velocity variations $\langle \Delta\Omega \rangle / \Omega_0 = \left(\langle \Omega \rangle - \{\Omega\} \right) / \Omega_0$ in cylindrical projection, elucidating the propagation of equatorial and polar branches of torsional oscillations. The color indicates faster rotation in red and slower rotation in blue, with departures of up to $\pm 10\%$ of the bulk rotation rate. (c) Time-latitude diagram of $\langle B_\varphi \rangle$ in cylindrical projection, exhibiting the equatorward migration of the wreaths from the tangent cylinder, and the poleward propagation of the higher latitude field, with the polarity of the field such that red (blue) tones indicate positive (negative) toroidal field.

with κ_r the molecular radiation diffusion coefficient, and c_P the specific heat at constant pressure. The entropy diffusion flux has the thermal eddy diffusivity κ acting on the entropy fluctuations. A calorically-perfect ideal gas equation of state is used for the mean state, about which the fluctuations are linearized as

$$\overline{P} = (\gamma - 1) c_\mathrm{P} \overline{\rho}\,\overline{T} / \gamma, \tag{9}$$

$$\rho / \overline{\rho} = P / \overline{P} - T / \overline{T} = P / \gamma \overline{P} - S / c_\mathrm{P}, \tag{10}$$

with $\gamma = 5/3$ the adiabatic exponent. The anelastic system of MHD equations requires 12 boundary conditions in order to be well posed. One of the primary goals of this work is to assess the generation of magnetic field and how it impacts the organization of angular momentum and energy in the simulation. Thus, the following impenetrable, torque-free, and flux transmitting boundary conditions are employed

$$v_\mathrm{r} = \frac{\partial}{\partial r}\left(\frac{v_\theta}{r}\right) = \frac{\partial}{\partial r}\left(\frac{v_\varphi}{r}\right) = \frac{\partial S}{\partial r} = 0, \quad \text{on } r = r_1 \text{ and } r_2. \tag{11}$$

The magnetic boundary conditions are perfectly conducting at the lower radial boundary (r_1) and matching to a potential field at the upper radial boundary (r_2), implying that

$$B_\mathrm{r}\big|_{r_1} = 0 \quad \text{and} \quad \mathbf{B}\big|_{r_2} = \nabla\Psi \Rightarrow \triangle\Psi = 0, \tag{12}$$

with Ψ the magnetic potential. The solution of Laplace's equation defines the three components of $\mathbf{B}$ at the upper boundary. Further details of the implementation and formulation of the ASH code can be found in Clune et al. (1999) and Brun et al. (2004).

Here a one solar mass star, with a solar luminosity, is considered that is rotating at three times the solar rate. An isentropic background stratification is employed that closely resembles the helioseismically-constrained Model S stratification (Christensen-Dalsgaard et al. 1996), with its normalized spherically-symmetric profiles of density ($\overline{\rho}$) and temperature ($\overline{T}$) shown in Figure 1(a). The simulated domain stretches from the base of the convection zone at $r_1 = 0.72\,\mathrm{R}_\odot$ to the upper boundary of the simulation at $r_2 = 0.97\,\mathrm{R}_\odot$, where $\mathrm{R}_\odot = 6.96 \times 10^{10}\,\mathrm{cm}$. This approximation omits the near-surface region and any regions below the convection zone, such as a tachocline. The simulation K3S has a resolution of $N_r \times N_\theta \times N_\varphi = 200 \times 256 \times 512$, corresponding to a horizontal resolution with a maximum spherical harmonic degree of $\ell_\mathrm{max} = 170$. In what follows, the operator $\langle\rangle$ indicates a longitudinal average (or mean) of a quantity, whereas the operator $\{\}$ indicates a longitudinal and temporal average. The extent of the temporal average varies depending upon the context of its use, so that interval will be indicated when the operator is invoked.

The SLD mechanism implemented in the ASH code, and used in case K3S, is similar to the schemes presented in Rempel et al. (2009) and Fan et al. (2013), though it has been modified to compensate for the grid convergence at the poles. This diffusive operator is detailed in Appendix A. SLD acts locally to achieve a monotonic solution by limiting the slope in each coordinate direction of a piecewise linear reconstruction of the unfiltered solution. The scheme minimizes the steepest gradient, while the rate of diffusion is regulated by the local velocity. It is further reduced through a function φ that depends on the eighth power of the ratio of the cell-edge difference $\delta_i q$ and the cell-center difference $\Delta_i q$ in a given direction i for the quantity q. This limits the action of the diffusion to regions with large differences in the reconstructed solutions at cell-edges. Since SLD is computed in physical space, it incurs the cost of smaller time steps due to the convergence of the grid at the poles, which is largely mitigated by introducing a filtering operator that depends upon latitude. The resulting diffusion fields are projected back into spectral space and added to the solution with a forward Euler time step.

The SLD has been restricted to act only on the velocity field in this simulation. This mimics a lower thermal and magnetic Prandtl number (Pr, Pm) than otherwise attainable through a purely Newtonian diffusion operator with the spatial resolution used in this simulation. Yet a weak viscous eddy diffusion is retained in addition to the SLD operator in order to reduce the condition number of the matrices used in ASH for the implicit Crank-Nicholson time stepping method. In contrast, the entropy and magnetic fields remain fully under the influence

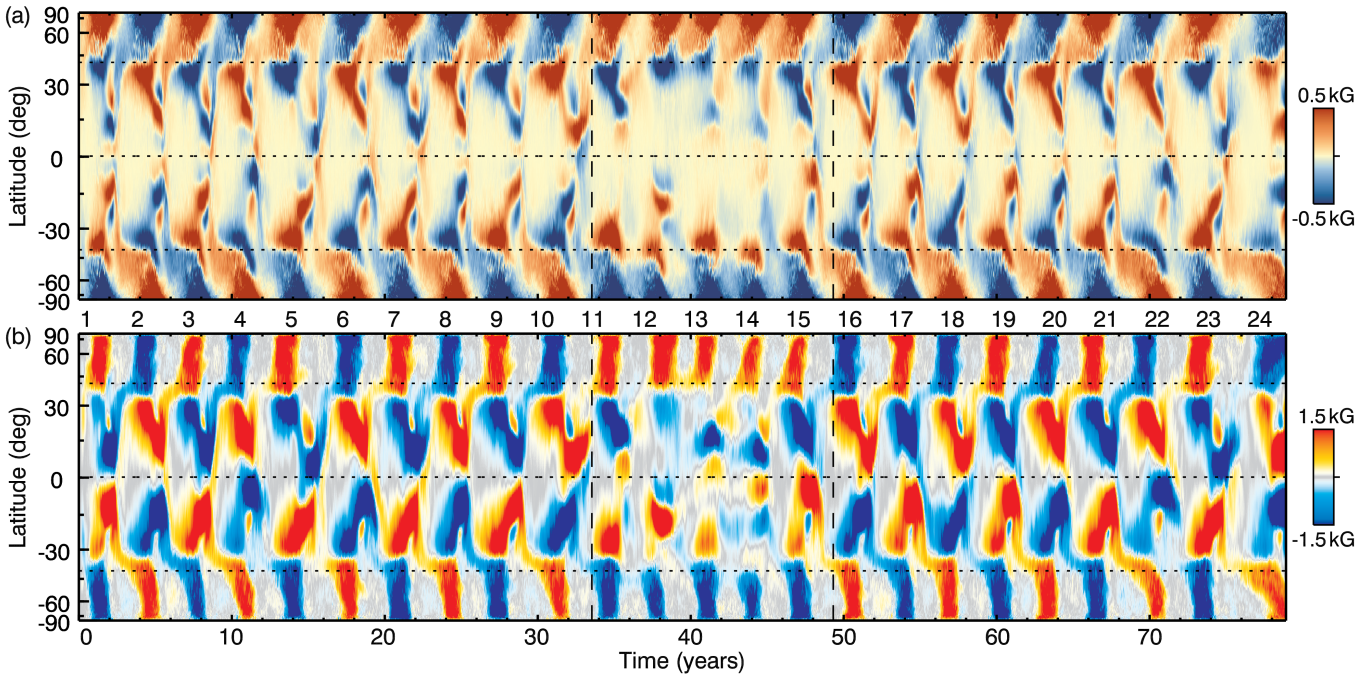

Figure 3. Evolution of the mean (longitudinally-averaged) radial $\langle B_r \rangle$ and toroidal $\langle B_\varphi \rangle$ magnetic fields over an extended interval of the K3S simulation, with its regular cycling interrupted by a grand minimum during the interval roughly between 33 to 49 years. (a) Time-latitude diagram of $\langle B_r \rangle$ at $0.92\,R_\odot$ in cylindrical projection, elucidating the poleward propagation of mid and high-latitude magnetic field and the equatorward propagation of lower latitude field. (b) Time-latitude diagram of $\langle B_\varphi \rangle$ at $0.92\,R_\odot$ in cylindrical projection, exhibiting the equatorward migration of the wreaths from the tangent cylinder (horizontal dotted lines at $\pm 43°$) and the poleward propagation of the higher latitude field. The polarity of the fields are such that red (blue) tones indicate positive (negative) field. The interval containing the grand minimum is marked by vertical dashed lines. Each magnetic energy cycle is labeled starting at unity.

of an eddy diffusion, with both a radially-dependent entropy diffusion κ and resistivity η. The eddy diffusion coefficients are roughly similar in form to those of case D3 from Brown et al. (2010) and case D3a Nelson et al. (2013a), with κ, ν, and $\eta \propto \overline{\rho}^{-1/2}$ and where the profiles of κ and η are shown in Figure 1(a). The value of these diffusion coefficients at the upper boundary are $\kappa(r_2) = 1.6 \times 10^{13}$, $\nu(r_2) = 4 \times 10^8$, and $\eta(r_2) = 8 \times 10^{12}$ with the units of each coefficient being $\mathrm{cm^2\,s^{-1}}$.

Since the majority of the viscous diffusion and dissipation is handled with the SLD scheme, it is somewhat involved to estimate standard fluid parameters such as the Reynolds number. However, a detailed analysis carried out in Appendix A.3 provides an estimate for the effective SLD viscosity. This also permits the estimation of the Reynolds number as $\mathrm{Re} \approx 350$, as well as thermal Prandtl number as $\mathrm{Pr} \approx 0.115$ and a magnetic Prandtl number of $\mathrm{Pr_m} \approx 0.23$. This is about a factor of two lower than in previous ASH simulations, which typically are carried out with $\mathrm{Pr} = 1/4$ and $\mathrm{Pr_m} = 1/2$. The effective magnetic Reynolds number is then $\mathrm{Re_m} = \mathrm{Pr_m Re_{eff}} \approx 90$. Further, the Rayleigh number can be characterized at mid-convection zone as $\mathrm{Ra} = \Delta \overline{S} g d^3 / c_P \nu \kappa \approx 6.3 \times 10^5$ and the Taylor number as $\mathrm{Ta} = 4\Omega_0^2 d^4/\nu^2 \approx 9.1 \times 10^7$, where $\Omega_0 = 3\,\Omega_\odot$ or $7.8 \times 10^{-6} \mathrm{rads^{-1}}$. The Rossby number, when defined with the enstrophy as $\mathrm{Ro} = |\nabla \times \mathbf{v}|/2\Omega_0$, varies with the magnetic cycle between 0.12 at magnetic maximum to 0.33 at magnetic minimum. Thus, some of these parameters differ significantly from other simulations that present features similar to this dynamo, namely those with equatorward propagating fields such as in Racine et al. (2011) and Warnecke et al. (2014) where the effective thermal and magnetic Prandtl numbers are between two and ten times larger. However, other relevant parameters are quite similar such as the effective Reynolds numbers as well as the Rayleigh, Taylor, and Rossby numbers.

3. OVERVIEW OF THE CYCLING DYNAMICS

With the formulation of the problem established, the discussion now turns to an overview of the dynamics occurring within the K3S simulation. A first diagnostic of the K3S simulation is to assess its cycles in a global sense. This is easily achieved by considering the evolution of volume-averaged energy densities of various components of the flow and magnetic field. The definition of the various energy densities are

$$\begin{aligned}
&\mathrm{DRE} = \frac{1}{2}\overline{\rho}\langle v_\varphi \rangle^2, \ \mathrm{MCE} = \frac{1}{2}\overline{\rho}\left(\langle v_r \rangle^2 + \langle v_\theta \rangle^2\right), \\
&\mathrm{CKE} = \frac{1}{2}\overline{\rho}\left(\mathbf{v} - \langle \mathbf{v} \rangle\right)^2, \ \mathrm{TME} = \frac{1}{8\pi}\langle B_\varphi \rangle^2, \\
&\mathrm{PME} = \frac{1}{8\pi}\left(\langle B_r \rangle^2 + \langle B_\theta \rangle^2\right), \ \mathrm{FME} = \frac{1}{8\pi}\left(\mathbf{B} - \langle \mathbf{B} \rangle\right)^2, \qquad (13)
\end{aligned}$$

where the total kinetic energy is DRE + MCE + CKE and the total magnetic energy is TME + PME + FME.

The periodic modulation of the kinetic energy in both the convection (CKE) and the differential rotation (DRE) can be seen in Figure 2(a), which covers the first 20 years of evolution of the simulation. Those changes are accompanied by the wax and wane of the energy contained in the magnetic field, though with a different temporal shift. The mean (longitudinally-averaged) toroidal magnetic fields (TME) contain the most magnetic energy, being formed by the action of the differential rotation on the poloidal magnetic field (e.g., §4.3). The nonaxisymmetric magnetic fields

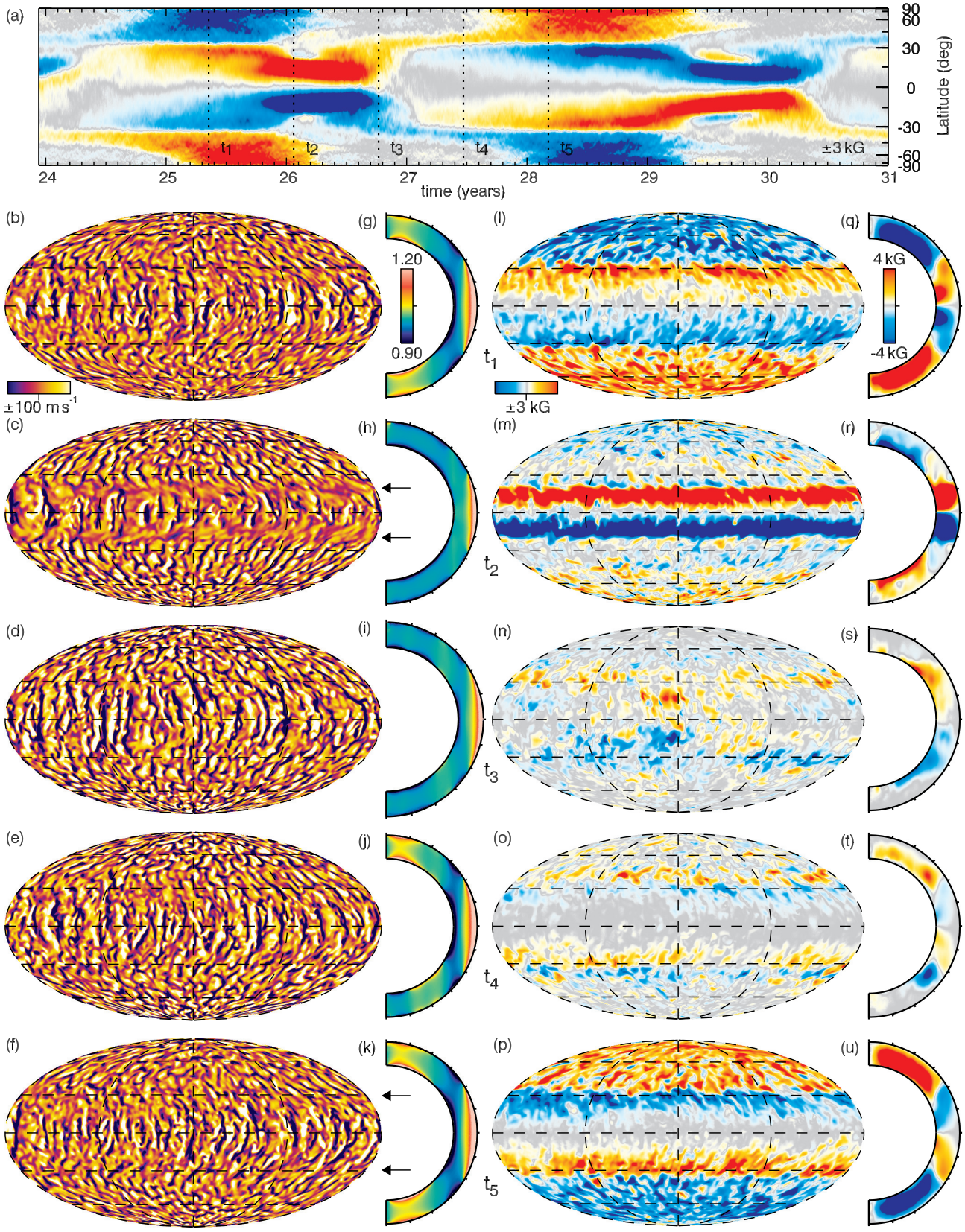

Figure 4. Changing velocity and magnetic fields during magnetic cycling. (a) The cylindrical projection of the mean toroidal magnetic field $\langle B_\varphi \rangle$ is shown with time and latitude at $0.90\,\mathrm{R}_\odot$ through the course of a full polarity cycle (capturing cycles 8 and 9), with colorbar as in (l). The times t_1 through t_5 are indicated with vertical dashed lines. (b)-(f) The horizontal structure of the radial velocity at $0.90\,\mathrm{R}_\odot$ is displayed in a global Mollweide projection (with dashed lines marking the equator and latitudes every 30°). The colorbar is given in (b). Downflows are darker tones and upflows lighter tones. Latitudes that are influenced by strong magnetic fields are indicated with arrows. (g)-(k) A 20-day-time and longitude-averaged angular velocity $\{\Omega\}/\Omega_0$ is shown in the meridional plane, with colorbar as in (g) where faster rotation is in red tones and slower in blue tones. (l)-(p) The longitudinal field B_φ at $0.90\,\mathrm{R}_\odot$ is illustrated, with the shared colorbar given in (l). (q)-(u) A 20-day-time and longitude-average of the toroidal magnetic field $\{B_\varphi\}$ is shown, with colorbar as in (q).

(FME) have the second greatest magnetic energy, whereas the mean (longitudinally-averaged) poloidal magnetic fields (PME) contain the least amount of magnetic energy. A double-peaked structure can be seen in the FME as well as in the TME. These variations in turn are largely due to the modulation of the differential rotation over the course of a cycle, which becomes readily apparent in Figures 2(b). Particularly, the pole and equator are accelerated as the system recovers from the quenching of the differential rotation that occurs during the magnetic maxima, leading to the first peak. There is also a phase difference in the peak in the magnetic energy between the deep and upper convection zones, which results in the second peak. The specific correlations and mechanisms that are behind this oscillatory behavior are covered below and in later sections.

The polarity reversals of the magnetic field are illustrated for the first 20 years of the simulation in Figure 2(c) and over an extended interval of the simulation in Figure 3. The magnetic field begins to regularly oscillate roughly every 3.1 years between positive and negative polarity states. Such regular cycling behavior arises shortly after the roughly 2 year kinematic growth phase of the magnetic fields, which began at year zero when this MHD simulation was initialized by inserting a dipolar magnetic field into a preexisting but mature hydrodynamic simulation. That initial magnetic field had a strength of about 100 G at the base of the convection zone. The initial energy in that magnetic field is about 10^5 times smaller than the total kinetic energy. The oscillations in the magnetic energy then continue throughout the entire evolution of the system. Throughout this paper two cycle periods will be cited. There is a 3.1 year magnetic energy cycle measured between maxima in the magnetic energy (or half-polarity cycle), which could be considered to be akin to the 11 year sunspot cycle. There is also a 6.2 year polarity cycle measured as the interval between magnetic maxima that have the same polarity as seen in Figure 3 for instance. This polarity cycle is akin to the 22 year solar polarity cycle.

The overall structure of the magnetic fields during a magnetic cycle is readily apparent in both Figures 3(a) and (b). The mean radial magnetic field ($\langle B_r \rangle$) is largely confined to higher latitudes, whereas the mean toroidal magnetic field field ($\langle B_\varphi \rangle$) has both prominent polar and low-latitude branches. At the radius where the magnetic fields in Figure 3 are sampled, the mean radial and toroidal magnetic fields differ by about a factor of three in magnitude. This ratio is approximately maintained throughout the domain, leading to the roughly order of magnitude difference between the toroidal and poloidal magnetic energies seen in Figure 2(a). There is an interval roughly between years 33 and 49 as seen in Figure 3 during which the system fails to fully reverse its polarity for five magnetic cycles. This interval will be referred to as a "grand minimum." While the choice of the beginning and end of this interval is somewhat arbitrary, this interval was chosen to be between the minimum in the magnetic energy near the upper boundary of the last "normal" cycle (near year 33, or cycle 11) and the similar minimum of the last abnormal cycle (near year 49, or cycle 16). The magnetic energy cycle is still operating during that interval, with the polar field waxing and waning but not fully reversing. However, the polarity cycles are disrupted at lower latitudes and the magnetic energy there is significantly reduced. This will be further explored in §5.

3.1. *Magnetic Energy Cycle in Detail*

Figure 4 illustrates the morphology of the convection, differential rotation, and the longitudinal magnetic fields in space and time over the course of a polarity reversal. Particularly, Figures 4(b)-(f) shows the convective patterns represented in radial velocities that are prevalent during different phases of the cycle (labeled as times t_1-t_5 in Figure (4)), with elongated and north-south aligned flows at low latitudes (banana cells) and apparently smaller scales at higher latitudes. Such flows are typical in the rotationally-constrained convection captured in global-scale large-eddy MHD simulations (e.g., Miesch et al. 2000; Käpylä et al. 2011b; Guerrero et al. 2013; Augustson et al. 2012, 2013). In aggregate, the velocity field of those rotationally-aligned convective cells produce correlations in the velocity field that yield strong Reynolds stresses that act to accelerate the equator and slow the poles. In concert with turbulent heat transport, such stresses serve to rebuild and maintain the differential rotation during each cycle. Indeed, when combined with the longitudinally-averaged Lorentz force and Maxwell stresses, those stresses induce the modulation in the angular velocity seen in Figures 2(b) and 4(g)-(k). The values of the shear do not quite reach zero, but are reduced by about 60% relative to their maximum value at lower latitudes. The elements of angular momentum transport that give rise to such modulation are further discussed in §4.2.

The presence of large-scale and longitudinally-connected magnetic structures is evident in B_φ as shown in Figures 4(l)-(p). Such toroidal structures have been dubbed wreaths (Brown et al. 2010). In this simulation, there are two evolving counter-polarized, lower-latitude wreaths that form in the region near the tangent cylinder at nearly all depths, meaning that the latitude of formation decreases with depth. This region is also where the peak in the latitudinal gradient of the differential rotation exists for much of a magnetic energy cycle (Figures 2(b) and 4(g)-(k)). In the latter set of figures, it is clear that the radial shear is roughly proportional to $r\sin\theta$ at low latitudes, for the differential rotation is largely cylindrical. Though, it tends decrease near the upper boundary. So for figures showing radial cuts, a radius of $0.92R_\odot$ was chosen to emphasize the region of greatest shear as it corresponds to the depth where $d\Omega/dr$ is largest.

There are also polar caps of magnetism that possess a magnetic polarity that is reversed compared to that of the low-latitude wreaths. These caps act to moderate the polar differential rotation, which would otherwise tend to accelerate and hence establish fast polar vortices. The average structure of the wreaths and caps at each point in the cycle is apparent in $\{B_\varphi\}$ exhibited in Figures 4(q)-(u), which is averaged over 20 days at each time t_i. The wreaths appear rooted at the base of the convection zone, whereas the caps have the bulk of their energy in the lower convection zone above its base. As will be seen in §6.1, the wreaths are initially generated higher in the convection zone while the wreath generation mechanism (primarily the Ω-effect) migrates equatorward and toward the base of the convection zone over the course of the cycle. The equatorward migration takes place largely in the upper convection zone nearer the beginning of the cycle at times t_1 and t_2. At later times, the mean toroidal magnetic field near the base of the convection zone migrates poleward and begins to build up the polar magnetic caps, which have a polarity opposite to the flux generated at lower latitudes. This represents a very different dynamo mechanism relative to a typical flux-transport dynamo.

The changes in the structure of the convection seen in Figure 4 plays a role in the dynamo, for they induce changes in

the Reynolds stress and the electromotive force (EMF) that generates the magnetic field. As a cycle proceeds, the magnetic fields disrupt the alignment and correlations of the convective cells through Lorentz forces, which is particularly evident in Figure 4(c). The presence of the magnetic fields, in addition to modifying the structure of the low-latitude convection, modulates the global convective amplitudes as might be ascertained by comparing Figures 4(b)-(f). Particularly, while the magnetic field gathers strength during a cycle, the strong longitudinally-connected magnetic fields also create a thermal shadow, weakening the thermal driving of the equatorial cells, as indicated with arrows.

Such influences of the magnetic fields on the convection and its ability to transport heat are also apparent, albeit less directly, in Figure 1(b) where the enthalpy, entropy diffusion, and kinetic energy fluxes are modulated by about 30% throughout a cycle. These fluxes vary largely in phase with the cycle, where at magnetic maximum the fluxes are smallest and near minimum they are largest. The reduction of the convective amplitudes also leads to the angular momentum transport of the flows being diminished as the magnetic fields become stronger (see §4.2). The effects of the magnetic fields on the convection are also captured in the ebb and flow of the kinetic energy contained in the nonaxisymmetric velocity field, which here varies by about 50% over the magnetic energy cycle (CKE in Figure 2(a)). Indeed, signatures of such in-phase magnetically-modulated convection have also been detected in EULAG-MHD simulations (Cossette et al. 2013; Charbonneau 2014). These magnetic feedback mechanisms are in keeping with the predicted impacts of strong longitudinal fields in the convection zone suggested by Parker (1987).

There is also the direct impact of the large-scale Lorentz forces on the differential rotation (e.g., the Malkus & Proctor (1975) effect). This process and the magnetic influences on the convection described above combine to explain why the differential rotation seen in Figure 2(b) cannot be fully maintained during the cycle. Rather, the angular velocity has substantial variations throughout the cycle (Figure 2(a)), which are largely driven by the strong feedback of the magnetic fields (see §4.2 and Figure 5). Such strong nonlinear Lorentz force feedbacks are not without precedent, as they have been seen in previous convective dynamo simulations as well (e.g., Gilman 1983; Brun et al. 2004; Browning 2008; Brown et al. 2011).

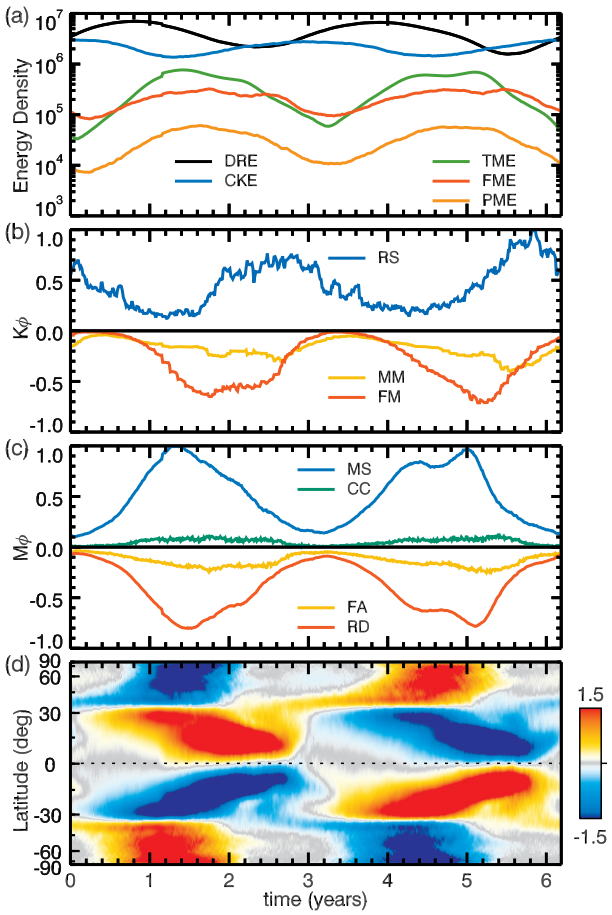

Figure 5. Energy densities and energy generation rates over the average polarity cycle. (a) Log-linear plot of the energy density of the differential rotation (DRE, black), nonaxisymmetric flow (CKE, blue), toroidal magnetic field (TME, green), nonaxisymmetric magnetic field (FME, red), poloidal magnetic energy (PME, orange) in units of erg cm^{-3}. (b) Volume-integrated differential rotation energy generation rate (K_φ, as in Equation 14), with the rate due to Reynolds stresses (RS, blue), mean magnetic stresses (MM, yellow), and fluctuating Maxwell stresses (FM, orange). (c) Volume-integrated mean toroidal magnetic energy generation rate (M_φ, as in Equation 15), with the rate due mean shear (MS, blue), compressive motions (CC, green), fluctuating advection (FA, yellow), and resistive diffusion (RD, red). In (b) and (c), the values are normalized by the maximum absolute value of the generation rates. (d) The cycle and longitude-averaged toroidal magnetic field $\langle B_\varphi \rangle$ evaluated over the average magnetic polarity cycle shown at 0.92 R$_\odot$, with a color bar given in units of kG.

4. ANATOMY OF A REVERSAL

The analysis of dynamical elements contributing to regular magnetic polarity cycles is aided by building a composite of a number of our regular cycles. This composite omits the interval designated as the grand minimum.

4.1. *Average Polarity Cycle*

The average polarity cycle is shown in Figure 5, which has been formed by identifying the common structures in each polarity cycle, obtaining the times of the beginning and end of each polarity cycle as defined through these structures, and then stretching each polarity cycle to be the same length in time and co-adding them. The statistical significance of this process is greatly aided by the regularity of the magnetic polarity cycle period, which typically varies by only about 10% of the average polarity cycle period (see §7). In particular, Figure 5(a) shows the time evolution of the relevant volume-integrated components of the total energy density. The differential rotation energy (DRE) is the largest component of the total kinetic energy followed by the kinetic energy in the convection (CKE). The energy contained in the meridional circulation is the smallest component, being roughly three orders of magnitude smaller than the DRE and is omitted from Figure 5(a). Such a small contribution of the meridional flow to the overall kinetic energy is typical of global-scale convection simulations (e.g., Brown et al. 2008; Augustson et al. 2012; Brun et al. 2014).

The total magnetic energy at its peak is about 30% of the total kinetic energy, or about 50% of the CKE, placing the K3S dynamo close to equipartition when averaged over the cycles and the domain. There are certainly some cycles and most certainly some regions in the computational domain in which the kinetic and magnetic energies are near equipartition. The bulk of the magnetic energy resides in the low-latitude magnetic wreaths and polar caps (TME), with the energy in the nonaxisymmetric field (FME) a close second. The energy contained

in the mean poloidal field (PME) is about an order of magnitude smaller.

Figure 5(a) further elucidates three prominent phase shifts, one between the differential rotation and the convection, a second between the magnetic field and the differential rotation, and a third between the convection and the magnetic field. The first phase shift is apparent when comparing peak values of CKE and DRE, where the CKE precedes the DRE by about a year. The second shift has the peak in DRE preceding that of TME by about 0.6 years. Finally, there is an additional phase shift between maxima of CKE and TME, with CKE preceding TME by about 1.5 years. Each of these phase shifts are related to the nonlinear coupling of the convective Reynolds stresses, the differential rotation, the Lorentz forces and the Maxwell stresses as will be further studied in §4.2 and 4.3.

The magnetic energy cycles visible in Figure 3 can be numbered starting with unity at year zero and extending up to cycle 24 at year 80. There are quantifiable differences between the even and odd-numbered magnetic energy cycles over that extended interval that become more apparent in the averaged polarity cycle shown in Figure 5. Such a temporal parity is similar to the observed behavior of the sunspots known as the Gnevyshev-Ohl rule (e.g., Charbonneau 2010). Those asymmetries are reflected in the behaviors exhibited by the energy densities and their transport mechanisms in the average polarity cycle shown in Figure 5. The average of the odd-numbered cycles are captured there as the first 3.1 year interval, and the average even cycle is shown over the succeeding 3.1 year interval. In particular, there is a deeper minimum in the magnetic energy densities as the odd-numbered cycles are entered as compared to the the entrance of the even-numbered cycles. When TME and PME are assessed alone, the deeper minima become more apparent, with their energy densities being about 50% and 25% lower respectively (Figure 5(a)). Such temporal differences in the properties of the odd and even cycles are also evident in the transport mechanisms. For instance the Reynolds stresses and Maxwell stresses of the odd cycles have a broader variation in time than the even cycles, where they are more sharply peaked in both of those quantities (Figure 5(b)). In contrast, the magnetic energy production terms exhibit the opposite correlation, with the production terms being more peaked during the even-numbered cycles (Figure 5(c)). Yet this simulation must be run longer to better assess the statistical significance of this temporal asymmetry. However, similar signatures of such differences between even and odd magnetic cycles have been found within the long-running cycles of an EULAG-MHD simulation (Passos & Charbonneau 2014).

4.2. *Maintaining the Differential Rotation*

The evolution of the energy contained in the differential rotation is critical to the behavior of the K3S dynamo, and its evolution is considered explicitly here. A detailed derivation of Equation 14 is given in Appendix B. In particular, it is shown in Appendix B that the boundary fluxes of mean kinetic energy of the longitudinal flows are zero as is the volume integrated energy arising from the advection of the angular velocity. Therefore, the evolution of the volume-integrated differential rotation kinetic energy (DRE) is

$$K_\varphi = \frac{d\mathrm{DRE}}{dt} = \int_V dV \frac{\partial}{\partial t}\frac{1}{2}\overline{\rho}\langle \mathrm{v}_\varphi\rangle^2 = \int_V dV \left[\overbrace{\overline{\rho}\lambda\langle \mathbf{v}'_\varphi \mathbf{v}'\rangle \cdot \boldsymbol{\nabla}\langle\Omega\rangle}^{\mathrm{RS}} - \overbrace{\frac{\lambda}{4\pi}\langle B_\varphi\rangle\langle\mathbf{B}\rangle \cdot \boldsymbol{\nabla}\langle\Omega\rangle}^{\mathrm{MM}} - \overbrace{\frac{\lambda}{4\pi}\langle B'_\varphi \mathbf{B}'\rangle \cdot \boldsymbol{\nabla}\langle\Omega\rangle}^{\mathrm{FM}} \right]. \quad (14)$$

with $\mathbf{v}' = \mathbf{v} - \langle\mathbf{v}\rangle$ the nonaxisymmetric velocity, $\mathbf{B}' = \mathbf{B} - \langle\mathbf{B}\rangle$ the nonaxisymmetric magnetic field, as well as $\langle\mathbf{v}\rangle$ and $\langle\mathbf{B}\rangle$ the axisymmetric velocity and magnetic field respectively.

Figure 5(b) shows the evolution of the primary components contributing to the dissipation and production of differential rotation kinetic energy (DRE) given in Equation (14). Clearly, the Reynolds stresses (RS) are the only significant means of producing DRE. The contribution of the SLD viscous stresses are very small when integrated over the volume, being over two orders of magnitude less than the RS. Thus they are not shown. The contribution of the RS to the DRE varies substantially throughout a cycle, which is a reflection of the Lorentz force impacting the morphology of convective structures that can be formed and thus their capacity to generate DRE. The magnetic fields do not play just a passive role either, for they actively dissipate and transfer energy as well. Indeed, both the mean magnetic stresses (MM) and the fluctuating Maxwell stresses (FM) contribute to the global transfer of DRE to the magnetic energy reservoir where some of this energy will be dissipated via a resistive channel. More importantly, the FM can act to inhibit local turbulence and vortical motions, acting much like an anisotropic and inhomogeneous viscous dissipation, whereas the MM act primarily on the large-scale flows such as the differential rotation. The FM dominate throughout much of the cycle, though the MM play a larger role during minima. Nevertheless, the amplitudes of the FM and MM during a magnetic energy cycle are tightly correlated with the magnetic energy densities, as expected.

The Reynolds stresses (RS) reach a peak about 0.4 years before a magnetic minimum and then begin to decrease through the minimum and the rest of the cycle (Figure 5(b)). If it were primarily the magnetic fields that modify the RS, one might expect that the RS terms would be maximum at the minimum of the magnetic energy. Instead, the RS are maximum when the differential rotation is at a minimum. There are likely two reasons for this: one is that the energy in the convection is growing at that time, leading to an increase in the RS, and the other is that the shear of the differential rotation itself modifies the velocity correlations of the convective structures. The shear of the differential rotation will radially and longitudinally stretch the equatorial columns of convection (banana cells) that are primarily responsible for building it. This tends to diminish the velocity correlations responsible for generating the Reynolds stresses.

4.3. *Building Toroidal Magnetic Structures*

The coherent large-scale wreath-like magnetic structures have been realized in many stellar convective dynamo simulations utilizing very different codes such as in Browning et al. (2006); Brown et al. (2008); Ghizaru et al. (2010); Käpylä et al. (2012); Augustson et al. (2013), and Nelson et al. (2013a). The common feature shared by all those simulations is that the regions in which the wreaths form in the convection zone is typically one where the Rossby number is

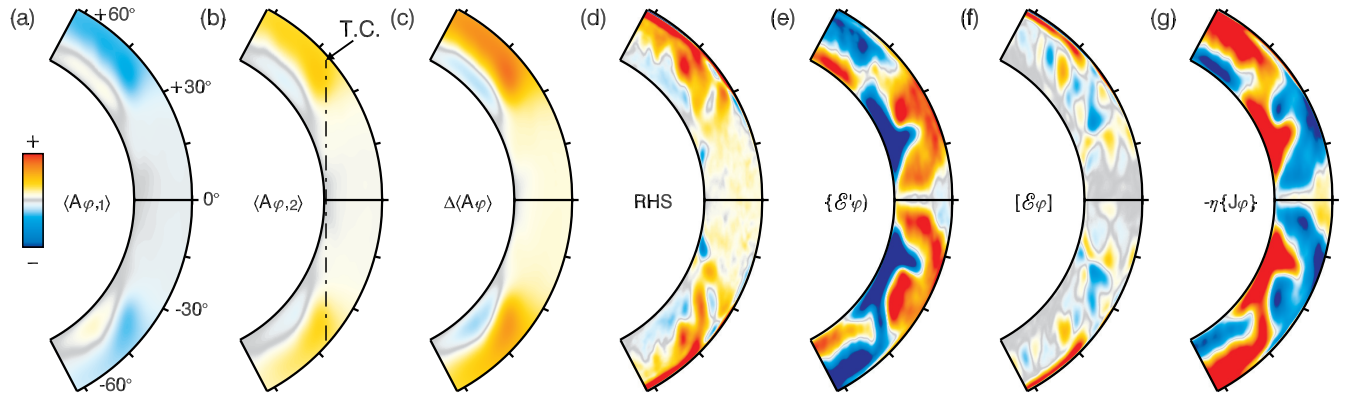

Figure 6. Time evolution of poloidal magnetic potential $\langle A_\varphi \rangle$ through a typical magnetic energy cycle. Longitudinal component of the magnetic potential (a) at t_1 called $\langle A_{\varphi,1} \rangle$ and (b) t_2 called $\langle A_{\varphi,2} \rangle$, and their difference (c) $\langle \Delta A_\varphi \rangle = \langle A_{\varphi,2} \rangle - \langle A_{\varphi,1} \rangle$. The sum of the right-hand-side terms in Equation (17) is shown as panel (d). The components of the sum are shown individually as: (e) the turbulent EMF $\{\mathcal{E}'_\varphi\}$, (f) the mean EMF $\left[\mathcal{E}_\varphi\right]$, and (g) the resistive diffusion $-\eta\{J_\varphi\}$. The location of the tangent cylinder (T. C.) is shown in (b).

low. For the ASH simulations, another feature that appears to promote the formation of longitudinal magnetic structures is a perfectly conducting lower boundary condition, which requires the field to be horizontal there. Thus the formation of magnetic wreaths in the K3S simulation is generally promoted both through its relatively low Rossby number as well as through the use of perfectly conducting lower boundary condition. These mean toroidal magnetic fields $\langle B_\varphi \rangle$ are shown in Figures 2, 3, and 4. Such magnetic fields are initially generated and subsequently maintained by similar processes. During the growth phase of the magnetic field, the shear of the differential rotation acts to fold and wind the initial poloidal field into large-scale longitudinal magnetic structures. In this kinematic phase, the shear and meridional flows are largely unaffected and can be considered stationary relative to the time scales of the growing field. However, once the magnetic fields are strong enough, they begin to impact the convective flows that cross them through Lorentz forces. Hence, the magnetic field strength becomes saturated as the back-reaction of the Lorentz forces increases the alignment of the velocity field and the magnetic field, which reduces both its generation and can lead to its destruction. To quantify these processes, consider the time evolution of the toroidal magnetic energy (TME), which can be represented as

$$M_\varphi = \frac{d\mathrm{TME}}{dt} = \int_V dV \frac{\partial}{\partial t} \frac{\langle B_\varphi \rangle^2}{8\pi} \tag{15}$$
$$= \int_V dV \frac{\langle B_\varphi \rangle}{4\pi} \hat{\boldsymbol{\varphi}} \cdot \Big[\overbrace{\langle \mathbf{B} \rangle \cdot \boldsymbol{\nabla} \langle \mathbf{v} \rangle}^{\mathrm{MS}} + \overbrace{\langle \mathbf{B}' \cdot \boldsymbol{\nabla} \mathbf{v}' \rangle}^{\mathrm{FS}} - \overbrace{\langle \mathbf{v} \rangle \cdot \boldsymbol{\nabla} \langle \mathbf{B} \rangle}^{\mathrm{MA}}$$
$$- \overbrace{\langle \mathbf{v}' \cdot \boldsymbol{\nabla} \mathbf{B}' \rangle}^{\mathrm{FA}} + \overbrace{\left(\langle \mathbf{B} \rangle \langle \mathrm{v_r} \rangle + \langle \mathbf{B}' \mathrm{v_r}' \rangle \right) \frac{\partial \ln \overline{\rho}}{\partial r}}^{\mathrm{CC}} - \overbrace{\boldsymbol{\nabla} \times \left(\eta \langle \mathbf{J} \rangle \right)}^{\mathrm{RD}} \Big].$$

A detailed derivation of the production terms for the mean magnetic fields in spherical coordinates is provided in Appendix A of Brown et al. (2010). The terms in Equation (15) are the production of magnetic energy by mean shear (MS), fluctuating shear (FS), mean advection (MA), fluctuating advection (FA), compressive correlations (CC), and resistive diffusion (RD).

The significant volume-integrated components of Equation (15) are shown in Figure 5(c). As suggested above, the Ω-effect or mean shear (MS) here is the dominant means of producing magnetic energy in the toroidal fields, which is accompanied by a weak contribution from the compressive terms (CC). In contrast, resistive dissipation (RD) and fluctuating advection (FA) dissipate TME. The other terms comprise less than 5% of the total production or dissipation of TME. While there is a generation of TME when all the terms are summed during much of the magnetic energy cycle, it is clear that much of the temporally local generation through mean shearing effects (or the Ω-effect) is counter-balanced by dissipative processes. As with the poloidal generation mechanisms as seen in §4.4, the generation of field is greater than its rate of dissipation during the growth phase of the energy cycle, as to be expected of a convective dynamo whose magnetic Reynolds number is supercritical. Whereas during the declining phase of the cycle, dissipation dominates these processes and so the magnetic energy declines. There is also a strong correlation between the generation of field through the compressive mechanism and dissipation by fluctuating advection. Their amplitudes are, however, not perfectly matched. Instead, the energy dissipated through the FA term is energy that is converted into either mechanical energy or magnetic energy such as the poloidal and nonaxisymmetric magnetic fields. Note that the magnetic energy dissipation through the FA term provides a first indication that the dynamo operating in K3S is of an α-Ω type rather than α^2-Ω within the context of mean-field dynamo theory (e.g., Krause & Raedler 1980). Indeed, the dissipative character of the FA term is more reminiscent of the diffusive mean-field β effect, which is defined in §8.

4.4. *Generating Poloidal Fields*

The time evolution of the magnetic field can be recovered from the magnetic vector potential, where for instance the mean toroidal magnetic vector potential $\langle A_\varphi \rangle$ captures the poloidal magnetic field as $\langle \mathbf{B}_P \rangle = \boldsymbol{\nabla} \times (\langle A_\varphi \rangle \hat{\boldsymbol{\varphi}})$. In particular, the behavior of $\langle A_\varphi \rangle$ is governed by the following form of the induction equation

$$\frac{\partial \langle A_\varphi \rangle}{\partial t} = \hat{\boldsymbol{\varphi}} \cdot \left[\langle \mathbf{v}' \times \mathbf{B}' \rangle + \langle \mathbf{v} \rangle \times \langle \mathbf{B} \rangle - \eta \langle \mathbf{J} \rangle \right]. \tag{16}$$

In what follows, $\boldsymbol{\mathcal{E}} = \mathbf{v} \times \mathbf{B}$ is the electromotive force (EMF). Thus the turbulent electromotive force (EMF, $\boldsymbol{\mathcal{E}}'$) is defined as $\langle \boldsymbol{\mathcal{E}}' \rangle = \langle \mathbf{v}' \times \mathbf{B}' \rangle$. The diffusion is proportional to the product of the current $\mathbf{J} = c/4\pi \boldsymbol{\nabla} \times \mathbf{B}$ and the magnetic diffusion

coefficient η. As noted in Nelson et al. (2013a), the definite time integral of this equation subsequently yields

$$\Delta\langle A_\varphi\rangle = \langle A_{\varphi,2}\rangle - \langle A_{\varphi,1}\rangle = \{\mathcal{E}'_\varphi\} + \left[\mathcal{E}_\varphi\right] - \eta\{J_\varphi\}$$
$$= \int_{t_1}^{t_2} dt\hat{\boldsymbol{\varphi}}\cdot\langle \mathbf{v}'\times\mathbf{B}'\rangle + \int_{t_1}^{t_2} dt\hat{\boldsymbol{\varphi}}\cdot\left(\langle\mathbf{v}\rangle\times\langle\mathbf{B}\rangle\right) - \int_{t_1}^{t_2} dt\eta\langle J_\varphi\rangle. \quad (17)$$

where $\left[\mathcal{E}_\varphi\right]$ denotes the time integral of the mean component of the EMF. This can be interpreted as the difference between two snapshots of the longitudinal vector potential being proportional to three time-integrated terms: the longitudinal-average of the turbulent EMF, the mean EMF, and the magnetic diffusion. Since only $\langle A_\varphi\rangle$ is being considered, Equations (16) and (17) are rendered gauge invariant since $\partial_\varphi\langle A_\varphi\rangle = 0$.

The mechanisms that set the time scales relevant to the reversal of the poloidal field are difficult to assess. Namely, these mechanisms require information about the collective action of the turbulent convection upon existing magnetic structures as well as the complex self-interaction of convection to produce differential rotation. These processes are inherently nonlocal in space as magnetic energy from the local and small-scale action of helical motions upon a large-scale toroidal magnetic structure leads to a large-scale poloidal field, and thus is also nonlocal in time as the large-scale structures evolve on longer time scale than the convection. However, these processes can be individually assessed, beginning with an illustration of the several components of the production of poloidal magnetic field. To help further disentangle the various influences of the convection on the turbulent production of magnetic field, a mean-field analysis of the K3S dynamo is provided in §8.

The terms in Equation (17) are shown in Figure 6, where the times t_1 and t_2 in Equation (17) are taken at the peak values of the magnetic energy on either side of a minimum in magnetic energy. Thus a magnetic energy cycle and a magnetic polarity reversal are captured. In order, Figure 6 shows the two instances of the vector potential (Figures 6(a), (b)) whose difference (Figure 6(c)) closely corresponds to the sum of the time-integrated components of the EMF and the magnetic diffusion, which are shown individually in the last three panels. Comparing Figures 6(e, g), the predominant competition is between the fluctuating EMF and the resistive diffusion, with a modest contribution from the mean EMF (Figure 6(f)) contributing to the full sum (Figure 6(d)).

Despite the large degree of cancellation between the fluctuating EMF and the resistive dissipation, the two act together to reverse the polarity of the poloidal field. In particular, the fluctuating EMF provides the dominant means of reversing the vector potential at lower latitudes (outside the tangent cylinder), whereas the resistive dissipation dominates at the higher latitudes (inside the tangent cylinder). Such an arrangement is largely due to the disparate spatial scales of the convection present in the magnetic field inside and outside the tangent cylinder, with the more easily dissipated smaller scales being prevalent at higher latitudes. There is also a temporal lag with the generation of the turbulent EMF and the later action of the magnetic diffusion. Nonetheless, at high latitudes and close to the upper boundary, the mean EMF makes a significant contribution to reversing the magnetic vector potential. This portion of the mean EMF is predominantly due to the poleward meridional flow in that region, namely $\langle \mathrm{v}_\theta\rangle\langle B_\mathrm{r}\rangle$. This term must dominate as the longitudinal average of the radial velocity is quite small in this near-surface high-latitude region due to the cancellation of small-scale convective flows and due to the impenetrable boundary condition. This influence of the meridional flow suggests that some aspects of a flux-transport dynamo could be operating in the near-surface region of this

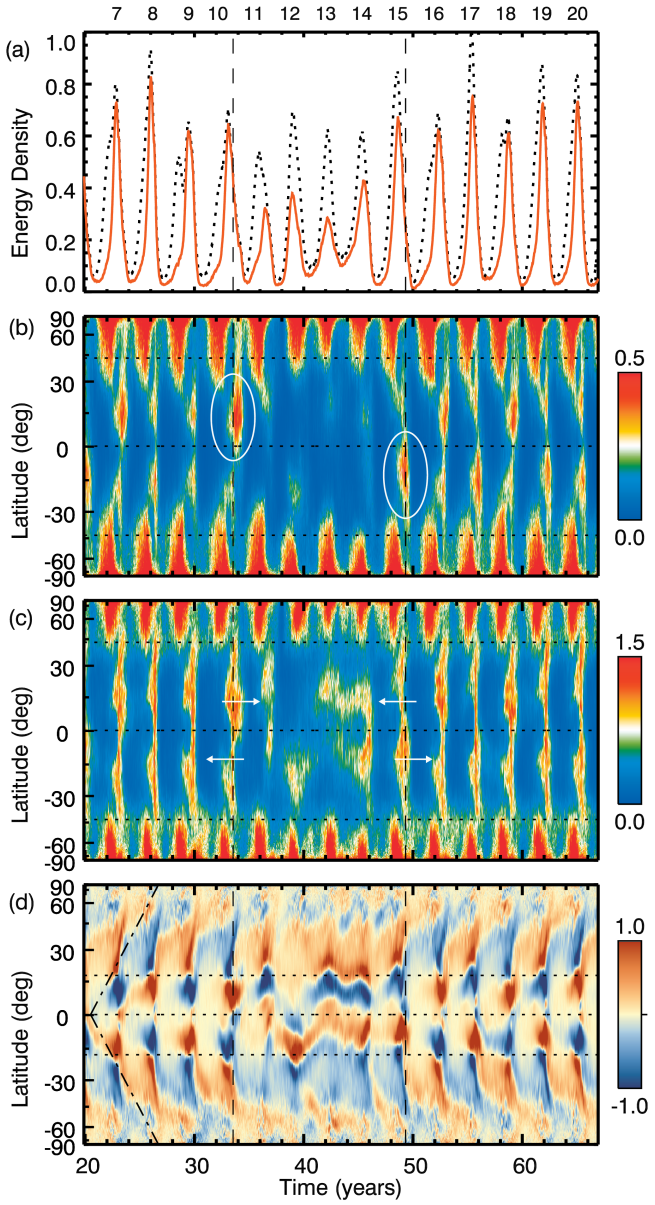

Figure 7. Evolution of total magnetic energy, nonaxisymmetric magnetic energy, and radial magnetic field through the grand minimum. (a) Time variation of the magnetic energy through the grand minimum. The normalized and volume-averaged total magnetic energy is depicted with integrals taken over the total volume (dotted black line) and at lower latitudes between $\pm 40°$ (red line). (b) Time advance of the nonaxisymmetric magnetic field magnitude ($|B_r|$ for $m > 0$) at $0.95\,\mathrm{R}_\odot$, with regions of strong equatorially antisymmetry encircled. (c) Time and latitude dependence of the nonaxisymmetric magnetic field magnitude ($|B_r|$ for $m > 0$) at $0.75\,\mathrm{R}_\odot$, with hemispheric temporal lags indicated with arrows. (d) Time-latitude diagram of $\langle B_\mathrm{r}\rangle$ at a depth of $0.75\,\mathrm{R}_\odot$ with dot-dashed lines helping to illustrate the primary evolution of the polarity cycle. Units in (b), (c), and (d) are kG. The tangent cylinder is indicated with horizontal dotted lines and the grand minimum by vertical dashed lines.

simulation. However, the direction of the transport is reversed relative to a typical flux-transport dynamo.

5. CHARACTERIZING THE GRAND MINIMUM

Some 3-D convective dynamo simulations have attained magnetic cycles that also show a longer-term modulation in the amplitude of their peak magnetic energy (e.g., Brown et al. 2011; Augustson et al. 2013; Charbonneau 2013). The K3S simulation shows similar properties, though with the additional features of a significant disruption and later recovery of the magnetic polarity cycles. Indeed, Figures 3, 7, and 8 show different aspects of the dynamo during the 16 year interval in the evolution of case K3S in which the polarity cycles are substantially disrupted and the magnetic energy is reduced. The volume-averaged magnetic energy density at lower-latitudes is decreased by a factor of two (Figure 7(a)), which is reflected in the larger decrease in the magnetic energy in the longitudinal fields relative to the other energy components. During this "grand minimum," the quite regular and self-similar cycles seen prior to it are nearly lost. In particular, the mean radial magnetic field in the deep convection zone does not exhibit a polarity cycle at low-latitudes, whereas there is a semblance of a polarity cycle at higher latitudes (Figure 7(d)). In the upper convection zone, the higher-latitudes do not reverse their polarity, though the lower-latitudes do retain something akin to a polarity cycle (Figure 3(a)).

Despite those disruptions, both the spatial and temporal coherency of the cycles are recovered after this interval and persist for the last 30 years of the 80 year-long simulation. Due to the decrease in the volume-averaged magnetic energy density during this interval and because it retains it magnetic energy cycle of 3.1 years, it is fairly similar to observed characteristics of the Sun during an average grand minimum. The largest difference between what is being called a "grand minimum" here and the characteristics of the grand minima seen in cosmogenic isotope data is that the heliospheric magnetic field appears to have maintained the reversals of its dipolar mode and its magnetic energy apparently was reduced by roughly a factor of four during an average grand minimum (McCracken 2007).

5.1. *Entering and Exiting the Grand Minimum*

As the interval of reduced magnetic energy and disrupted cycles is entered, there is an anomalous excitation of low-m modes, where m is the longitudinal wavenumber. This event appears to be precipitated by an asymmetry of the magnetic field in time and relative to the equator (Figures 7(b), (c), (d)). The regions of strong magnetic field in the nonaxisymmetric modes are circled in Figure 7(b), and the direction of the hemispheric temporal lags are indicated by arrows in Figure 7(c). The atypical excitation of the nonaxisymmetric modes occurs near the end of cycle 10, during what should normally be a minimum in the magnetic energy. This likely disrupts the normally clean polarity reversals and may permit the longer-term excitation of the axisymmetric even-ℓ modes. Those even-ℓ modes are equatorially symmetric with $m = 0$, where ℓ is the spherical harmonic degree. Cycle 10, which begins near year 30, is an atypical magnetic energy cycle during which there is a strong cross-equatorial filament of radial magnetic field (Figure 3(a)) and where only the northern hemisphere exhibits a significant equatorward propagation (Figure 3(b), (d)). This led to a substantial temporal lag between the northern and southern hemispheres throughout the magnetic energy cycle. While the precise physical mechanisms that yield such a state are ambiguous, the symmetric modes of the radial magnetic field were strongly excited as the grand minimum is entered at year 33 (Figures 7(c) and 8(b)). Furthermore, the subsequent four energy cycles of the grand minimum do not fully reverse the odd-ℓ axisymmetric modes, whereas some of the even-ℓ axisymmetric modes do begin to reverse (particularly at depth).

Given the larger contribution of the even modes during the grand minimum, the Ω-effect (or $\langle \mathbf{B}_P \rangle \cdot \nabla \langle \Omega \rangle$) is less efficient at building and maintaining strong longitudinal magnetic fields through latitudinal shear. However, the symmetric modes of the radial magnetic field can influence the dynamo at low latitudes, where the differential rotation has a strong radial gradient due to the cylindrical rotation profile. Hence during the grand minimum, the longitudinal magnetic field is largely generated by radial shear rather than by latitudinal shear. Both the radial magnetic field and the radial gradient of the angular velocity tend to be weaker than their latitudinal counterparts, leading to the weaker longitudinal magnetic fields seen during this grand minimum. Moreover, as was shown in Strugarek et al. (2013), the primary influence on the dipolar mode is the differential rotation, whereas the quadrupolar mode was fed energy through coupling to small-scale convection. Such nonlocal couplings may also be at work in K3S as well. Such differences in the primary inverse energy cascades of the dynamo are indicative of the sensitivity of the dynamo to the symmetry of the convection as well as the magnetic field.

There is a decay of the even modes and an increase in the energy of the odd modes throughout the magnetic energy cycles of the grand minimum, as indicated with dashed lines in Figures 8(a) and (b). This likely permits the exit from the grand minimum near year 49 into another interval of regular equatorially antisymmetric cycles. These regular magnetic energy cycles involve a prominent alternation in the peak energy of the even modes between successive magnetic energy cycles. Cycle 15 possesses the first such high peak after the grand minimum. Indeed, it appears that the entrance into and the exit from the grand minimum are heralded by the excitation of the even modes of the poloidal magnetic field (Figure 8(b)). Such findings are not without precedent, as similar issues regarding the relative influence of higher-order multipole modes and their interactions within magnetic dynamos have been discussed (e.g., Tobias 1997; Brandenburg & Spiegel 2008; Nishikawa & Kusano 2008; Gallet & Pétrélis 2009; DeRosa et al. 2012; Karak & Choudhuri 2013). What is unique here are the strongly excited low-m modes and the temporal lag between the hemispheres, during the cycles that are active as the grand minimum is entered and exited. These atypical events appear to excite the symmetric dynamo modes and diminish the influence of the antisymmetric modes throughout the grand minimum.

5.2. *Dynamo Families and Magnetic Field Parity*

The interplay of the antisymmetric (primary) and symmetric (secondary) dynamo families and their parity has some precedent within the context of the solar dynamo as explored in DeRosa et al. (2012). Rather than attempting to assess the behavior of each mode to quantify how these two dynamo families interact within the K3S simulation, it is useful to construct a more encompassing measure of all the modes involved in the dynamo. One such measure is the parity of the radial magnetic field, which provides a scalar indication of the rel-

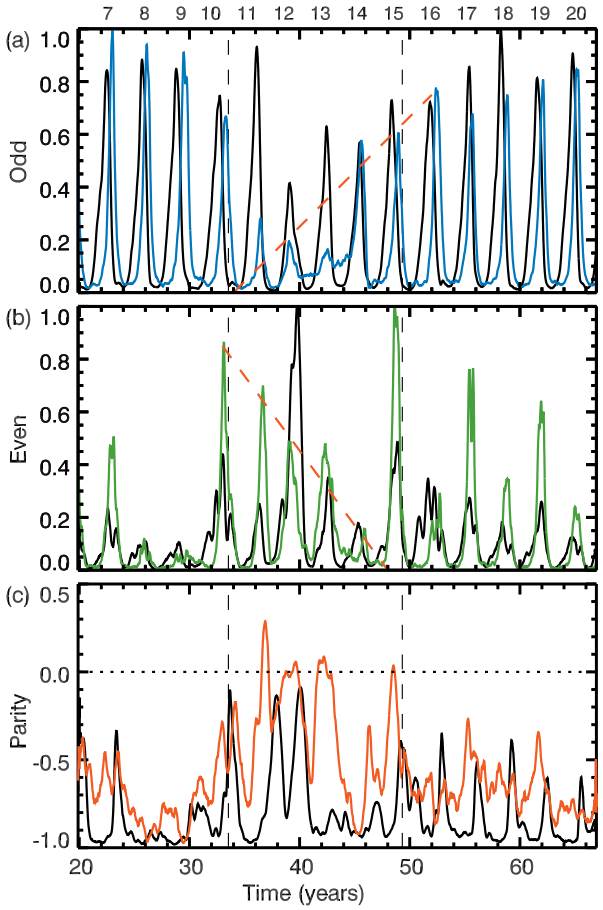

Figure 8. Time variation of the radial magnetic energy through the grand minimum at two depths. (a) Power in odd ℓ, $m = 0$ modes of $B_r^2/8\pi$ at a depth of $0.75\,R_\odot$ (blue) and $0.95\,R_\odot$ (black). (b) Power in even ℓ, $m = 0$ modes of $B_r^2/8\pi$ at a depth of $0.75\,R_\odot$ (green) and $0.95\,R_\odot$ (black). The red dashed lines in (a) and (b) indicate the general trends of the magnetic energies. (c) Magnetic parity, showing the dominance of odd parity during normal cycles and more even parity during the minimum at two depths ($0.75\,R_\odot$ orange, $0.95\,R_\odot$ black), indicating that even parity becomes prominent at depth entering and during the grand minimum.

ative importance of the symmetric and antisymmetric modes for each longitudinal wavenumber m and radius r. It is defined as

$$\mathcal{P}(r,m) = \frac{B^2_{\rm even}(r,m) - B^2_{\rm odd}(m)}{B^2_{\rm even}(r,m) + B^2_{\rm odd}(r,m)}, \qquad (18)$$

$$B^2_{\rm even}(r,m) = \sum_{\substack{\ell+m \\ \rm even}} |B_r(r,\ell,m)|^2\,,\; B^2_{\rm odd}(r,m) = \sum_{\substack{\ell+m \\ \rm odd}} |B_r(r,\ell,m)|^2\,,$$

with ℓ the spherical harmonic degree. When this parity measure is negative, the radial magnetic field favors an equatorially antisymmetric state, whereas a positive parity indicates that the radial magnetic field is in a symmetric state. The axisymmetric ($m = 0$) parity of the radial magnetic field in case K3S is usually large and negative as is illustrated by Figure 8(c), meaning that the system strongly prefers most of the energy being in the antisymmetric (odd-ℓ) modes during typical cycles. In the near-surface region this is especially true, as it possesses an average magnetic parity of –0.9. The magnetic parity in the deeper convection zone is also quite negative being –0.7 on average, when the grand minimum is omitted from that average. In contrast, the nonaxisymmetric modes (those with $m > 0$) show no parity preference, where their near-zero parity is maintained during both typical cycles and during the grand minimum.

During regular polarity cycles, there is also a distinct phase delay between the peak in magnetic energy in the odd-ordered modes at depth and those near the surface, as seen in Figure 8(a). Furthermore, it shows that the reversal in the odd-ordered modes usually occurs later at depth than it does near the surface, indicating the top-down nature of the poloidal magnetic field reversal. In contrast, the even-ordered modes show no such phase discrepancies. Yet in Figure 8(b), there is a prominent alternation in the peak energy of the even modes between successive magnetic energy cycles during the regular cycles after the grand minimum. Such behavior accounts for the similarity to the Gnevyshev-Ohl rule that those cycles seem to obey. However, prior to entering the grand minimum this pattern is lost, and it is only regained as the grand minimum is exited.

The three magnetic energy cycles prior to entering the grand minimum were all atypical. In particular, magnetic energy cycles 8 and 9 were more equatorially antisymmetric than a typical cycle, as indicated by the low magnitude of their even-ℓ axisymmetric modes (Figure 8(b)). The surface layers also reversed earlier than normal relative to when the magnetic fields in the deep convection zone reversed, being almost 2.5 years earlier instead of the average of one year (Figure 8(a)). This preceded cycle 10, where the lengthened minimum and reversal phase discrepancy were especially pronounced in the southern hemisphere. This breaks the pronounced equatorial antisymmetry of the magnetic field. Such a change in symmetry is largely maintained throughout the grand minimum, when the parity remains near zero. This indicates the stronger coupling of the symmetric and antisymmetric dynamo families within that interval. Indeed, throughout the grand minimum, both the deep convection zone and the upper convection zone have a significant contribution to the amplitude of the radial magnetic field from both the symmetric (even-ℓ) and antisymmetric (odd-ℓ) modes. In that interval, the ratio of the power in those modes remains close to unity within the convection zone, which is particularly evident in the deep convection zone as visible in the magnetic parity shown in 8(c).

The parity variations similar to those seen in Figure 8(c) have also been found and studied in nonlinear mean-field dynamo models (Tobias 1997; Moss & Brooke 2000; Brooke et al. 2002). In those studies, there is a clear variability of the parity of the dynamo models between the antisymmetric and symmetric modes, with the dynamo solution being often accompanied by a strong quadrupolar component. Such variability, which also leads to intervals of deep minima, confirms that the interplay between the dynamo families is critical to achieve intermittent and aperiodic dynamo states. These studies have further shown that low magnetic Prandtl numbers favor more irregular and time-dependent solutions with extended intervals of minimal activity. Similarly the SLD treatment used for the K3S simulation, by favoring lower magnetic Prandtl number dynamos, is likely at the origin of the appearance of the deep minimum described above. In the Moss & Brooke (2000) and Brooke et al. (2002) studies, the symmetric dynamo modes can become completely dominant. In contrast, the symmetric dynamo modes do not fully become dominant in the K3S simulation. Rather, it is likely that the interplay of the two dynamo families leads to the grand minimum

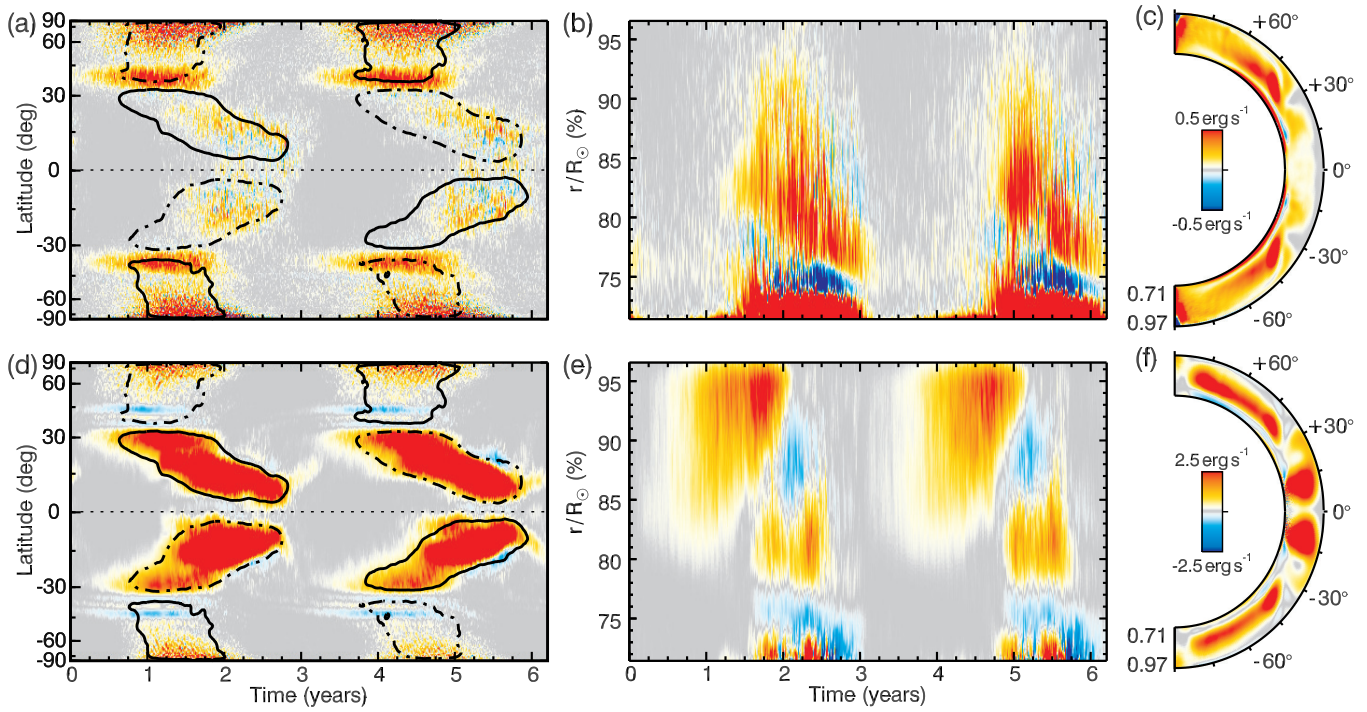

Figure 9. Comparison of the evolution of the mean poloidal magnetic energy production through the fluctuating EMF (P_{FL}) and mean toroidal magnetic energy production by mean shear (T_{MS}) over the average polarity cycle. An overlay of the contours $\langle B_\varphi \rangle$ at 500 G is also shown, with solid contours being of positive polarity and dash-dotted of negative polarity. (a) Mean poloidal magnetic energy generation P_{FL} at $0.92\,\mathrm{R}_\odot$ shown with latitude and time in cylindrical projection, illustrating the strong field generation above about $\pm 30^\circ$ and the weak generation that accompanies the equatorward propagation of the toroidal wreaths. (b) P_{FL} plotted with depth $r/\mathrm{R}_\odot$ at a latitude of 25°. The tapering with depth arises from the strong radial dependence of $\mathbf{B}_P$, with a downward direction of propagation. (c) P_{FL} averaged over the magnetic energy cycle rendered in the meridional plane. (d) Mean toroidal magnetic energy generation T_{MS} exhibited over the average cycle and with latitude in cylindrical projection at $0.92\,\mathrm{R}_\odot$, showing the equatorward migration of field generation. (e) T_{MS} in depth and time at a latitude of 25°, with two zones of migration evident. (f) T_{MS} averaged over a magnetic energy cycle, where the equatorial and polar regions represent spatially separated zones of generation. The color bars are shared between (a)-(c) and (d)-(f).

and the return to the regular magnetic cycles captured in the low magnetic Prandtl number regime realized here.

6. EQUATORWARD PROPAGATION OF MAGNETIC WREATHS

Having now studied how the regular cycles could be disrupted, it is appropriate to analyze in further detail how the magnetic energy is generated in both space and time. This will also show how the equatorward propagation may arise in K3S.

6.1. *Spatio-Temporal Evolution of Dynamo Mechanisms*

As will be seen in §8, the K3S simulation is most akin to an α-Ω mean-field dynamo, requiring an assessment of the two dominant modes of magnetic energy generation. These modes are the generation of poloidal magnetic energy through the fluctuating EMF (the α-effect, e.g., Moffatt (1978)) and the generation of mean toroidal magnetic energy through the differential rotation (Ω-effect) acting on the mean poloidal magnetic field. The first mechanism is denoted $\langle P_{\mathrm{FL}} \rangle = \langle \mathbf{B_P} \cdot \nabla \times \mathcal{E}'_\varphi \hat{\boldsymbol{\varphi}} \rangle$ and the second $\langle T_{\mathrm{MS}} \rangle = \lambda \langle B_\varphi \rangle \langle \mathbf{B}_P \rangle \cdot \nabla \Omega$. What is also of note, had the generation of the magnetic field been instead shown, nearly identical propagating patterns and correlations are seen.

In Figure 9, two primary regions of production of poloidal magnetic field are visible: one at low latitudes and another at high latitudes. The low-latitude regions of poloidal energy production are associated with convective cells acting upon the equatorially migrating magnetic wreaths. While the mechanism is somewhat similar for the high-latitude poloidal field, it primarily originates in the helical action of convection on the polar caps. The primary source of magnetic energy for those caps of toroidal magnetic field is the more rapidly rotating poles, which are established during the magnetic minimum as seen in Figures 2 and 4.

The spatial and temporal separation of mean poloidal and toroidal field generation is particularly evident when comparing Figures 9(a) and 9(d). The greatest generation of poloidal field is concentrated in the polar regions and near the tangent cylinder, with the low latitudes playing much less of a role. In contrast, the generation of mean toroidal magnetic field is greatest at low latitudes throughout the bulk of the cycle. In Figures 9(b) and 9(e), there is a relatively thin region in radius where the sign of the poloidal magnetic energy generation rate reverses. This sign reversal is largely due to the change in the sign of the kinetic helicity of the convection that occurs near the base of the convection zone. Such a kinetic helicity reversal is expected due to the influence of the lower boundary (e.g., Miesch et al. 2000), which has an impact on the α-effect as will be discussed in §8.

The beginning of each magnetic energy cycle in Figure 9 occurs at years 0.0 and 3.1, when the magnetic fields are weakest. At those times, the toroidal and poloidal magnetic fields begin to grow at roughly $\pm 30^\circ$ (Figures 2(c), 3, 9(a), (d)). The turbulent action of the convection on this newly generated wreath sustains the poloidal field generation through

P_{FL} on the high-latitude edge of the wreath, which is near the tangent cylinder. In combination with the polar EMF that emerges from the action of convection on the longitudinal fields there, this sustains the poloidal field that in turn allows the wreaths to be maintained through the shearing action of the differential rotation. However, once the polar differential rotation has been quenched, the toroidal magnetic fields begin to decay. Subsequently, the poloidal field generation that had been quite prominent at the tangent cylinder vanishes. The remaining generation of the poloidal field then moves equatorward, advancing with the migration of the wreaths. Yet that poloidal field generation is still largely on the high-latitude edge of the low-latitude wreaths. At this point, the strong longitudinal magnetic field at low latitudes has begun to significantly feedback on the equatorial differential rotation, modifying the structure of the convection and diminishing the differential rotation. Indeed, the centroid for the greatest dynamo action propagates equatorward and downward in radius as the magnetic energy cycle progresses, which is evident in the time-latitude diagram (Figure 9(a), (d)) and which is suggested in the time-radius diagram (Figure 9(b)). Hence, the equatorial migration begun at the surface makes its way deeper into the domain as the magnetic energy cycle advances.

The low-latitude wreaths of field eventually lose their coherence and energy through the lack of sufficient differential rotation to sustain them (e.g., Figure 2(b)), the destructive influence of the convection (Figure 7), and also due to cross-equatorial flux cancellation. Once those magnetic field structures have been sufficiently diminished, the diffusion and convection serve to rapidly redistribute the remaining magnetic flux. This is evident in Figures 3 and 4. As the end of each cycle is approached, the wreaths converge on the equator and their resulting destruction changes the morphology of the convective cells. The modified convective patterns better permit the poleward migration and diffusion of the surviving low-latitude magnetic field polarity. Such actions lead to the topological reconnection of the large-scale magnetic field. This migrating field is of the opposite sense compared to the previous cycle's polar cap. Being of greater amplitude compared to the remaining polar magnetic field, those fields establish the sense of the subsequent cycle's polar field. Thus the polarity of the subsequent magnetic field seems to be determined by the EMF generated at the equator, as was also seen in Augustson et al. (2013) and Nelson et al. (2013a). This source of poloidal magnetic field begins to be generated once the toroidal magnetic fields are sufficiently close to the equator to enable a strong cross-equatorial interaction. It is sustained throughout the rest of the cycle. During this period, the origin of this poloidal field generation is the action of convection on the low-latitude edge of the wreaths.

6.2. *Kinematic Versus Nonlinear Dynamo Waves*

The equatorward propagation of magnetic features observed in this simulation, which is visible in Figure 2(b) and the broad panorama of Figure 3(b), will now be assessed to disentangle which mechanisms permit such behavior. The equatorward propagation in kinematic α-Ω dynamo models is traditionally attributed to the propagation of a dynamo wave. In kinematic theory the propagation direction of such a wave is given by the Parker-Yoshimura rule (e.g., Parker 1955; Yoshimura 1975) as

$$\mathbf{S} = -\lambda\overline{\alpha}\hat{\boldsymbol{\varphi}} \times \boldsymbol{\nabla}\frac{\Omega}{\Omega_0}, \tag{19}$$

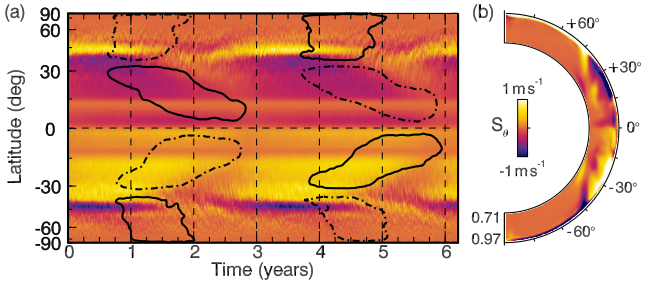

Figure 10. The latitudinal component of the propagation direction of a dynamo wave, corresponding to Equation (19) with $\overline{\alpha} = \alpha_{(\varphi\varphi)}$. (a) Latitudinal propagation velocity S_θ shown over an average polarity cycle at $0.92\,\mathrm{R}_\odot$ with time and latitude. An overlay of the contours $\langle B_\varphi \rangle$ at 500 G is also shown, with solid contours being of positive polarity and dash-dotted of negative polarity. (b) The latitudinal propagation $\{S_\theta\}$ averaged over the polarity cycle and shown in the meridional plane. Dark tones indicate negative latitudinal propagation, light tones positive latitudinal propagation.

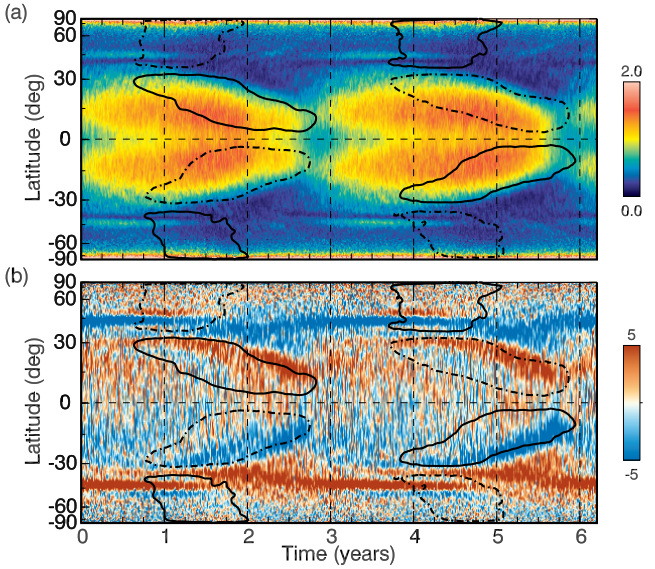

Figure 11. Coevolution of the mean toroidal magnetic field $\langle B_\varphi \rangle$ at $0.92\,\mathrm{R}_\odot$ over the average magnetic polarity cycle with (a) the magnitude of the mean angular velocity gradient $\mathrm{R}_\odot\,|\nabla\Omega|/\Omega_0$ and (b) latitudinal velocity $\langle \mathrm{v}_\theta \rangle$ of the evolving meridional circulation in units of $\mathrm{m\,s^{-1}}$. Here $\langle B_\varphi \rangle$ is overlain with positive magnetic field as solid lines and negative field as dashed lines, with the contours corresponding to a 500 G strength field.

where $\lambda = r\sin\theta$ and $\overline{\alpha} = -\tau_o\langle \mathbf{v}' \cdot \boldsymbol{\omega}' \rangle/3$, with $\boldsymbol{\omega}' = \boldsymbol{\nabla} \times \mathbf{v}'$. Thus $\overline{\alpha}$ depends on the convective overturning time τ_o and the kinetic helicity. When Lorentz-force back-reactions are taken into account, there is also a current helicity contribution to $\overline{\alpha}$ (e.g., Pouquet et al. 1976; Gruzinov & Diamond 1994). Augustson et al. (2014) demonstrated that the kinematic expression in Equation 19 with $\overline{\alpha}$ defined using only the kinetic helicity fails to explain the equatorward propagation seen in this dynamo simulation. The current helicity can in principle reverse the sign of the scalar α-effect (Warnecke et al. 2014). For instance, it has recently been shown that the direction of the propagation of the magnetic field through a cycle can depend upon the Parker-Yoshimura mechanism (e.g., Racine et al. 2011; Käpylä et al. 2013; Warnecke et al. 2014).

Rather than explicitly including the current helicity here, $\overline{\alpha}$ can be procured from the simulation itself. As described in §8, the full α tensor is obtained from an SVD decomposition.

When the scalar α-effect utilizes information from that derived α tensor, it will automatically include information about both the current and kinetic helicities. Hence, the $\alpha_{(\varphi\varphi)}$ component of the α tensor is used in place of $\overline{\alpha}$ in Equation 19 to determine the propagation direction of the dynamo wave predicted by mean-field theory. This is shown in Figure 10. With such a definition of $\overline{\alpha}$, the Parker-Yoshimura sign rule still does not hold for this simulation. More precisely, the sign of the latitudinal propagation of a dynamo wave is of the opposite sign required for both the equatorward migration of low-latitude magnetic structures and the poleward propagation of magnetic field as seen in Figure 10. So, although the Parker-Yoshimura mechanism seems to be at work in other convective dynamo simulations (Racine et al. 2011; Warnecke et al. 2014), it does not appear to be operating here.

Thus, another mechanism must be sought to explain the equatorward propagation in the K3S simulation. In contrast to the intuition derived from mean-field theory, the dominant mechanism appears to be the nonlinear feedback of the magnetic fields upon the differential rotation. The tight correlation between the presence of B_φ and the angular velocity gradient $|\nabla\Omega|$ is demonstrated in Figure 11(a). Since the latitudinal shear serves to build and maintain the magnetic wreaths (as in §4.3), the latitude of peak magnetic energy corresponds to that of the greatest shear. So the region with available shear moves progressively closer to the equator as the Lorentz forces of the wreaths locally weaken the shear (Figure 11(a)). Hence the appearance of equatorward motion in K3S is attributed to a nonlinear dynamo wave. This interpretation is consistent with the substantial modulations of the differential rotation seen in Figure 2 and the equatorward migration of the toroidal source term shown in Figure 9. In a mean-field dynamo, the equatorward propagation of the toroidal source term arises from the equatorward propagation of the poloidal magnetic field. Here, the equatorward propagation of $\nabla\Omega$ also contributes.

Accompanying the local weakening of the gradient of the differential rotation is a meridional flow that is gyroscopically induced at the poleward edge of the low-latitude magnetic wreaths as seen in Figure 11(b), with gyroscopic pumping defined as in McIntyre (1998) and Miesch & Hindman (2011). In particular, the torque provided by the divergence of the Lorentz force and the Maxwell stresses produce a change in the local shear which in turn induces a change in the meridional flow. Indeed the spatio-temporal correlation between the changing differential rotation, the mean toroidal magnetic field, and the meridional flow seen in Figure 11 appears to support a nonlinear dynamo wave. This mechanism for producing an equatorward migration of magnetic field relies upon the complex dynamical coupling of the differential rotation, meridional flows, and the magnetic field.

7. ASSESSING THE CYCLE PERIODS

A correlation analysis of the dominant processes in this simulation is useful to quantitatively ascertain the magnetic and polarity cycle periods and the correlations. Such analysis also permits the estimation of the variance of those cycles. First consider the dynamical coupling of the mean magnetic fields $\langle\mathbf{B}\rangle$ and the mean angular velocity $\langle\Omega\rangle$, which plays a crucial role in regulating the magnetic energy cycle. The significant spatial and temporal correlation between $\langle B_\varphi\rangle$ and angular velocity variations $\langle\Delta\Omega\rangle$ during reversals is apparent when comparing Figures 2(a) and 2(b), and it is readily seen in Figure 11(a), revealing the strong nonlinear coupling of the magnetic field and the differential rotation.

7.1. *Correlation Analysis*

The dynamics that couples the differential rotation and the mean toroidal magnetic field is captured in two terms: the mean toroidal magnetic field generation due to mean shear ($S = \lambda\langle\mathbf{B}_P\rangle\cdot\boldsymbol{\nabla}\langle\Omega\rangle$, with $\langle\mathbf{B}_P\rangle$ the mean poloidal field) and the azimuthal component of the mean Lorentz-force $Q = \hat{\boldsymbol{\varphi}}\cdot\langle\boldsymbol{\nabla}\times\langle\mathbf{B}\rangle\rangle\times\langle\mathbf{B}\rangle$, which acts on the longitudinal component of the momentum equation (Equation (2)). As shown in Figure 12(a), the auto-correlation of each of these components of the MHD system reveals that Q varies with a period corresponding to the magnetic energy cycle, whereas S is self-correlated over the polarity cycle period. Similarly, the cross-correlation between $P_{\rm FL}$ and $T_{\rm MS}$ indicates their close temporal correlation. There is, however, a phase lag of about $0.05\tau_{\rm M}$ or 2 months between the two primary energy generation mechanisms for the mean toroidal and poloidal magnetic fields (Figure 12(b)). Yet there is also a high degree of temporal regularity between cycles, with the auto-correlation of both quantities remaining significant with 95% confidence for a single polarity cycle and with 67% confidence for three such cycles as indicated by the shaded areas of Figures 12(a), (b). To further quantify the regularity of the cycles one could consider the full-width half-maximum of the auto-correlation of S and Q as well as the cross-correlation of $P_{\rm FL}$, and $T_{\rm MS}$ (Figure 12(b)). Indeed, an average of the FWHM of those correlated quantities yield a standard variance of the cycle period of about 4 months or about 10% of the magnetic energy cycle period of 3.1 years.

This analysis has been undertaken primarily to emphasize two basic features of the K3S dynamo. First, the time scale for the Lorentz-force feedback on the differential rotation, and hence the energy cycle time scale, is τ_M. This is the basic mechanism that sets the clock for the magnetic energy cycles. Second, the polarity cycle time τ_P is then twice the energy cycle time scale, which simply follows from the mathematical behavior of the square of a sinusoid being directly related to a sinusoid of twice of its period. To further illustrate the time scales that arise in this simulation, the volume-averaged frequency power spectrum of $\langle B_\varphi\rangle$ is shown in Figure 12(c). There is clear peak in the power spectrum around the average polarity cycle time τ_P of 6.2 years. The width of this peak gives a hint as to the variance of the magnetic polarity cycle period, which appears to be about one year. If the peak in power at τ_P is subtracted, then there is a nearly uniform distribution of time scales longer than about 2 years, potentially reflecting the aperiodic character of those time scales. The power at shorter time scales decreases roughly as the inverse square of the frequency, which is common in the pink noise of highly complex and nonlinear systems. There is also a broad peak at time scales corresponding to the convective overturning time of about 25 days, or 0.07 years.

7.2. *Potential Time Scales*

In addition to the primary identification of these time scales, the processes assessed in previous sections suggest that there at least two processes that lead to those time scales. One is the effective rate of conversion of differential rotation kinetic energy into mean toroidal magnetic energy (τ_Ω). The second is the time required to diffuse magnetic field from the equator to the pole (τ_η). A third potentially relevant time scale is related to the rate at which the magnetic field converges toward the equator may also be important. This in turn can be related to the gyroscopically-pumped meridional circulation induced

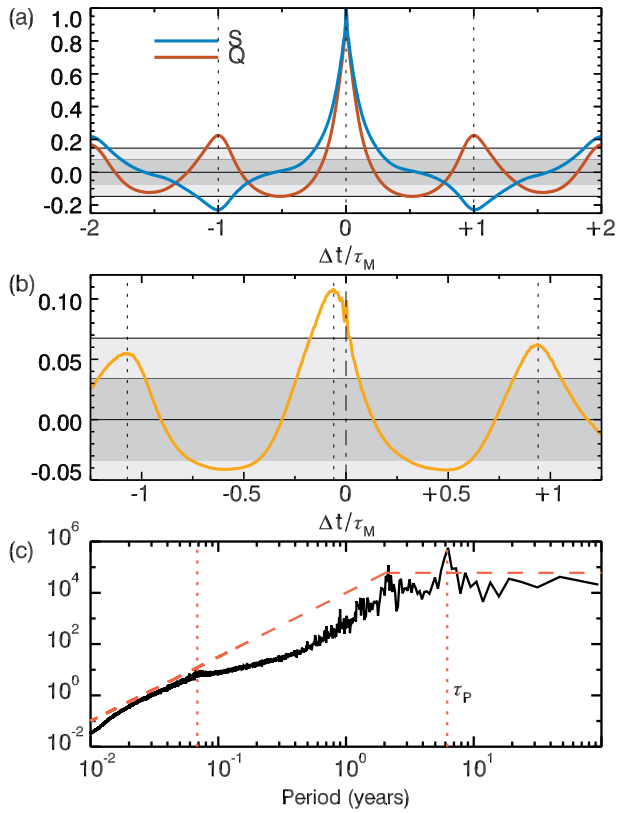

Figure 12. Auto and cross-correlation of Lorentz-force and mean toroidal magnetic field production by mean-shear. (a) Volume-averaged temporal auto-correlation of mean toroidal magnetic field generation by mean shear (S, blue curve) and the same for the mean Lorentz force impacting the mean angular velocity (Q, red curve) plotted against temporal lags Δt normalized by the magnetic energy cycle period $\tau_{\rm M}$. Confidence intervals are shown as shaded gray regions, with the 67% interval in darker gray and 95% in lighter gray. (b) Cross-correlation of the mean poloidal energy production through the fluctuating EMF ($P_{\rm FL}$) and the mean toroidal magnetic energy production due to the mean shear ($T_{\rm MS}$). (c) The volume-averaged temporal power spectrum for $\langle B_\varphi \rangle$. The red vertical dotted lines indicate the convective overturning time of 0.07 years and the polarity reversal time scale of 6.2 years and the red dashed line indicates a $1/f^2$ pink noise spectrum.

by the changes in the magnetic fields as they approach the equator. The first time scale τ_Ω can be measured as

$$\tau_\Omega = \frac{2\pi}{\Delta\Omega}\frac{|\langle B_\varphi\rangle|}{|\langle \mathbf{B}_P\rangle|} \approx 3.6\,\text{years}. \qquad (20)$$

The diffusion time scale from the equator to the pole is

$$\tau_\eta = \frac{\pi}{2(r_2-r_1)}\int_{r_1}^{r_2}\frac{drr^2}{\eta} \approx 6.7\,\text{years}. \qquad (21)$$

Finally, the meridional circulation time scale follows from the average time it takes for an ensemble of particles to traverse a path of the meridional circulation in K3S or

$$\tau_{\rm MC} = \frac{1}{N_p}\sum_{\mathbf{p}_i}\oint_{\mathbf{p}_i}\frac{d\boldsymbol{\ell}\cdot\mathbf{v}_{\rm MC}}{\mathrm{v}_{\rm MC}^2} \approx 1.2\,\text{years}, \qquad (22)$$

where each particle path is denoted as $\mathbf{p}_i$. With these simple estimates of these relevant time scales, it is seen that the shear time scale and the diffusion time scale are close to the magnetic energy cycle period and to the magnetic polarity cycle respectively. However, since all three of these mechanisms are operating concurrently, a single time scale might emerge from their combined influence. One such way to accomplish this is to take the geometric mean of these time scales, which yields 3.1 years, which reflects the observed magnetic energy cycle period τ_M. This, however, only loosely suggests that these three processes may share in setting the magnetic energy cycle period as well as the polarity cycle period. Indeed, the shearing and the diffusion time scales alone are nearly adequate to explain the magnetic and polarity cycle time scales.

8. MEAN-FIELD ANALYSIS

The complex set of processes at work in this dynamo solution, as just assessed in §4 and 6.1, yield a dynamo that falls outside of the broad classes of α-Ω dynamos that underpin much of the mean-field theory (MFT) of MHD (e.g., Steenbeck et al. 1966; Moffatt 1978; Krause & Raedler 1980; Brandenburg & Subramanian 2005), which typically assume a temporally constant differential rotation and fluctuating EMF. Rather, the feedback of the magnetic field on both the nonaxisymmetric and axisymmetric components of the convective flows is critical to the operation of the dynamo running in this simulation. This suggests that, if one were to attempt to fully model these dynamics in the context of MFT, one would need to include an α-quenching mechanism and the Malkus-Proctor effect. Nevertheless, helical turbulent convection is largely responsible for the generation of poloidal field. As such, MFT provides a route to assess and quantify the various zeroth-order influences of the turbulent velocity field upon the generation of the turbulent electromotive force (EMF, $\boldsymbol{\mathcal{E}}'$). Thus a spatially varying, but temporally constant, and δ-correlated α-effect is now examined.

8.1. *Examining the Turbulent Electromotive Force*

As seen in §4.4 and §6.1, $\boldsymbol{\mathcal{E}}'$ is largely responsible for the generation of poloidal magnetic field in this simulation. Therefore, the generation of poloidal field will be characterized through the mean-field evolution of the mean toroidal vector potential $\langle A_\varphi\rangle$ as in Equation (17), which is gauge independent since it only considers longitudinally-averaged quantities. The connection between MFT and the EMF achieved in this simulation will be examined by noting that the first-order expansion of $\boldsymbol{\mathcal{E}}'$ around the mean magnetic field and its gradient is

$$\langle\boldsymbol{\mathcal{E}}'\rangle = \alpha\langle\mathbf{B}\rangle + \beta\nabla\langle\mathbf{B}\rangle + \mathcal{O}\left(\partial\langle\mathbf{B}\rangle/\partial t, \nabla^2\langle\mathbf{B}\rangle\right), \qquad (23)$$

where α is a rank two pseudo-tensor and β is a rank three tensor. In the following the β term will be neglected for simplicity. However, this does increase the systematic error in estimating the α tensor. A SVD decomposition that includes the β-effect has been undertaken in order to provide a lower bound on this systematic error. It is 21% when averaged over all components of the α tensor. In this analysis α has been expanded as $\alpha\langle\mathbf{B}\rangle = \alpha_S\langle\mathbf{B}\rangle + \boldsymbol{\gamma}\times\langle\mathbf{B}\rangle$, with α_S being the symmetric portion of α and $\boldsymbol{\gamma}$ the antisymmetric portion. The latter is also known as the turbulent pumping velocity (e.g., Krause & Raedler 1980; Käpylä et al. 2006). The diagonal components of α are automatically symmetric. Yet the symmetrized elements of α are all denoted as (ij).

To reconstruct the α tensor from the simulation data, its individual components are determined from a temporal sequence of data at each radial and latitudinal grid point using a method similar to the least-squares singular value decomposition (SVD) methodology described in Racine et al. (2011).

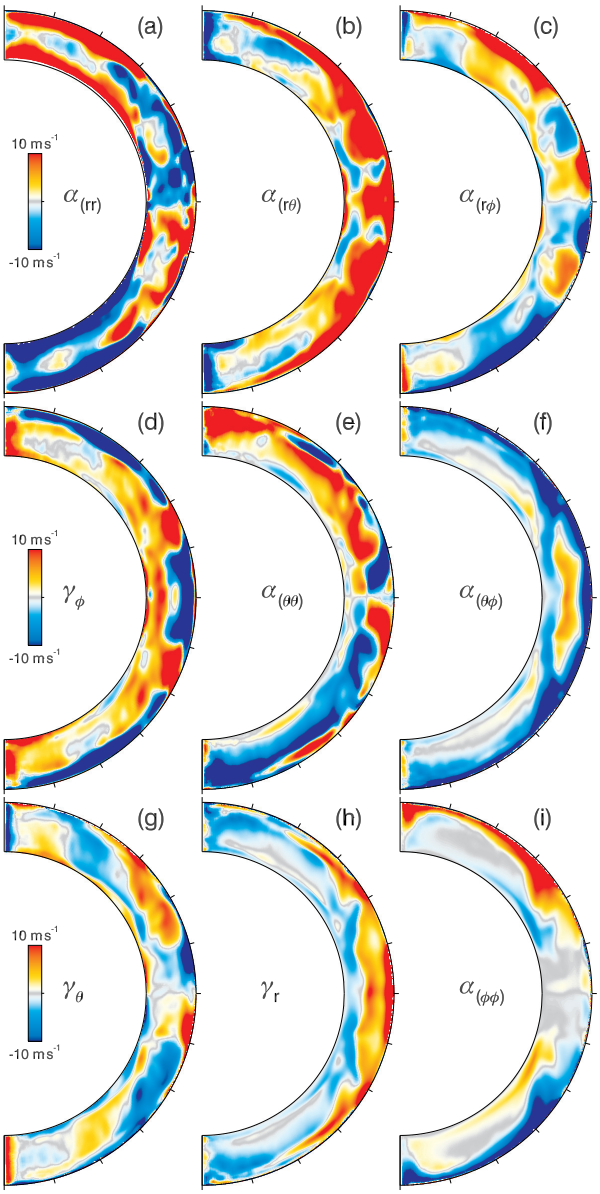

Figure 13. A mean-field theoretic interpretation of the dynamics. The nine components of the α tensor are shown, as computed using a SVD technique. The diagonal components of α are shown in (a), (e), and (i). The symmetrized components of the tensor are shown in (b), (c), and (f). The antisymmetric turbulent pumping components are shown in (d), (g), and (h). The colorbar and scaling are uniform across all panels.

Such a local fitting technique assumes that each point may be treated independently, which precludes the capture of temporal and spatial correlations that can influence the dynamo action (Brown et al. 2011; Nelson et al. 2013a; Augustson et al. 2013). Yet it has the advantage that the magnetic fields and electric currents from the simulation constrain the components of α. The reconstruction of α is carried out using the data from the extended interval of 80 years, as shown in Figure 3.

Figure 13 shows the nine components of α that contribute to $\langle \boldsymbol{\mathcal{E}}' \rangle$. The magnitude of the components of the α tensor are on par with other solar dynamo simulations (Racine et al. 2011; Nelson et al. 2013a; Simard et al. 2013). All of the α tensor components contribute to the generation of the magnetic vector potential through the turbulent EMF and thus to the poloidal and toroidal magnetic fields. The spatial structures of $\alpha_{(r\varphi)}$, $\alpha_{(\varphi\varphi)}$, and γ_θ visible in Figures 13(c), (g), and (i) are roughly antisymmetric between the two hemispheres, with the other two components $\alpha_{(\theta\varphi)}$ and γ_r being nearly north-south symmetric. The antisymmetry arises from the influence of Coriolis forces on the flows, with the cyclonic turbulence present at higher latitudes being an important contributor to the sign and magnitude of these fields. Such an arrangement is also indicative of the dipolar nature of the poloidal magnetic field, which has a symmetric latitudinal magnetic field and an antisymmetric radial magnetic field. Thus, it is not a surprise that the equatorially symmetric components of α are those that act on the latitudinal magnetic field. All of the components shown also have structures that reflect the global-scale properties of the convection zone (CZ), where there is a radial symmetry or antisymmetry about the middle of the CZ. This is particularly evident in $\alpha_{(\theta\varphi)}$ and $\alpha_{(\varphi\varphi)}$, where the divergence of vortical downflows and the convergence of swirling upflows gives rise to this feature. As might be expected, there is a latitudinal dependence to these structures, where a distinct transition in flow morphology occurs across the tangent cylinder.

Most of the features seen here are also present in the α tensor yielded in the analysis of an EULAG-MHD simulation shown in Racine et al. (2011). In particular, the components of the tensor possess a radial antisymmetry with respect to a radius related to the point at which the vorticity of the bulk of the flows reverses its sign, which is above the base of the convection zone. Moreover, the radial and longitudinal elements of α are latitudinally antisymmetric, much like the simulation here. The latitudinal components are symmetric reflecting the importance of the dipolar component of the magnetic field. Some of the tensor elements of the EULAG-MHD simulation may appear to differ by a sign relative to the α tensor seen in Figure 13. However, this is due to the use of latitude rather than co-latitude in displaying the results of Racine et al. (2011).

8.2. *The Efficiency of the α Effect*

An interesting measure of the dynamo is how efficiently the convective flows can regenerate existing mean magnetic fields. The dynamo efficiency of these flows can be surmised by finding the average magnitude of an estimated α-effect relative to the rms value of the nonaxisymmetric velocity field. One such measure of the dynamo efficiency E is

$$\langle \frac{\alpha}{v_{\rm rms}} \rangle \sim E = \frac{3}{2\left(r_2^3 - r_1^3\right)} \sum_{a,b} \iint \mathrm{d}r\mathrm{d}\theta r^2 \sin\theta \sqrt{\frac{\alpha_{ab}\alpha^{ab}}{\{\mathbf{v}' \cdot \mathbf{v}'\}}}, \quad (24)$$

where $\{\mathbf{v}' \cdot \mathbf{v}'\}$ is the sum of the diagonal elements of the Reynolds stress tensor averaged over the duration of the simulation and over all longitudes. For the K3S simulation, this measure yields a dynamo efficiency of 70%. If one considers only the generation of $\mathcal{E}'_\varphi$ by summing over only the components of $\alpha_{i\varphi}$, this efficiency measure yields 15%, which is half of the 30% value found for simulations of F-type stars (Augustson et al. 2013). Such a level of efficiency is what one might expect given the factor of five between the rate of mean toroidal magnetic energy generation and poloidal energy generation seen in Figures 9(c) and (f). One can utilize Equation 24 to provide a measure of the importance of each of the relative components of α as

$$\langle \frac{\alpha_{ij}}{v_{\rm rms}} \rangle \sim \epsilon_{ij} = \frac{3}{2E\left(r_2^3 - r_1^3\right)} \iint {\rm d}r{\rm d}\theta r^2 \sin\theta \sqrt{\frac{\alpha_{ij}\alpha^{ij}}{\{\mathbf{v}' \cdot \mathbf{v}'\}}}$$
$$= \begin{bmatrix} \epsilon_{(rr)} & \epsilon_{(r\theta)} & \epsilon_{(r\varphi)} \\ \epsilon_{\gamma_\varphi} & \epsilon_{(\theta\theta)} & \epsilon_{(\theta\varphi)} \\ \epsilon_{\gamma_\theta} & \epsilon_{\gamma_r} & \epsilon_{(\varphi\varphi)} \end{bmatrix} = \begin{bmatrix} 0.355 & 0.124 & 0.073 \\ 0.110 & 0.103 & 0.066 \\ 0.062 & 0.054 & 0.053 \end{bmatrix}. \quad (25)$$

Equation 25 clearly indicates that the $\alpha_{(rr)}$ component is dominant, with those processes contributing to $\alpha_{(rr)}$ being about 2.9 times more efficient than the next largest component $\alpha_{(r\theta)}$ and 6.7 times more efficient than the smallest component $\alpha_{(\varphi\varphi)}$. Indeed, the upper two by two matrix formed by $\alpha_{(rr)}$, $\alpha_{(r\theta)}$, $\alpha_{(\theta\theta)}$ and γ_φ possesses the terms that make the largest contribution to the α-effect. Specifically, these terms encapsulate those turbulent processes that are the most efficient at converting mean poloidal magnetic field into toroidal magnetic field. However, an assessment of the magnetic energy generating capacity of the α and Ω-effects requires a proper tensor norm of the relevant energy generation terms. Such an assessment also permits the characterization of the dynamo in the context of mean-field dynamo theory.

8.3. *Mean-Field Characterization of the Dynamo*

To assess which category of mean-field dynamos that the K3S dynamo falls into, one can measure the relative influence of the α effect to that of the Ω effect. In particular, the following ratio quantifies this

$$\frac{\alpha_\phi}{\Omega} = \frac{3}{2\left(r_2^3 - r_1^3\right)} \iint dr d\theta r^2 \sin\theta \left| \frac{\langle B_\varphi \rangle \hat{\boldsymbol{\varphi}} \cdot \boldsymbol{\nabla} \times \langle \boldsymbol{\mathcal{E}}' \rangle}{\lambda \langle B_\varphi \rangle \langle \mathbf{B}_P \rangle \cdot \boldsymbol{\nabla} \langle \Omega \rangle} \right|. \quad (26)$$

With this measure one can also quantify the impact of individual components of the α-effect that generates mean toroidal magnetic field. Overall, it is found that the α effect is 11.9 times smaller than the Ω effect. If each of the six terms in the numerator of Equation 26 are considered individually, it is seen that the term $\alpha_{(\theta\varphi)}$ is about 50% larger than the average of the other terms. Moreover, the terms in the longitudinal component of the α effect arising from $\mathcal{E}'_\theta$ are 43% larger than those from $\mathcal{E}'_r$. This implies first that the generation of toroidal magnetic field through the α-effect is weak and that those terms that contribute to that effect are dominated by the horizontal components of α.

The component $\alpha_{(\varphi\varphi)}$ effectively represents the action of helical convection on the mean toroidal magnetic field. In the context of the classical α-Ω dynamo, that term is usually taken to be the largest if not the only term in the α tensor. In the K3S dynamo this term has the smallest contribution, being about three times smaller than the components with the largest efficiency norm. However, it is also acting on the mean toroidal field, which is the largest component of the magnetic field. To quantify the efficacy of the poloidal field generation by the turbulent EMF relative to that of the toroidal magnetic field, consider the following measure

$$\frac{\alpha_P}{\alpha_\varphi} = \frac{3}{2\left(r_2^3 - r_1^3\right)} \iint dr d\theta r^2 \sin\theta \left| \frac{\langle \mathbf{B}_P \rangle \cdot \boldsymbol{\nabla} \times \langle \boldsymbol{\mathcal{E}}' \rangle}{\langle B_\varphi \rangle \hat{\boldsymbol{\varphi}} \cdot \boldsymbol{\nabla} \times \langle \boldsymbol{\mathcal{E}}' \rangle} \right|. \quad (27)$$

This average yields a ratio of 4.4 for the relative generation of poloidal and toroidal magnetic field through the α effect. This is consistent with the above argument that the α effect is relatively unimportant for the generation of the toroidal magnetic field.

It is evident that the impact of the convection upon the mean magnetic fields provides the primary regenerative mechanism for the mean poloidal field at low latitudes, while the diffusion of poloidal field is the primary mechanism operating at higher latitudes (see §4.4). In contrast, the mean toroidal magnetic fields are primarily built through the interaction of the mean poloidal magnetic field and the rotational shear. Therefore, given the presence of the differential rotation to sustain the mean toroidal magnetic field and the convective regeneration and diffusion of the poloidal magnetic field, this simulation could be characterized as an α-Ω dynamo. However, the non-local spatio-temporal correlations contained in the generation terms of the magnetic field in this simulation makes an exact characterization of the dynamo within the context of mean-field theory difficult. For instance, if this dynamo were simply a kinematic α-Ω dynamo, the Parker-Yoshimura mechanism should be sufficient to explain the equatorward propagation of magnetic field structures.

9. CONCLUSIONS AND DISCUSSION

The 3-D simulation K3S self-consistently exhibits five prominent features: (i) regular magnetic energy cycles during which the magnetic polarity reverses near the magnetic energy minimum; (ii) magnetic polarity cycles with a period of $\tau_P = 6.2$ years, where the equatorially antisymmetric modes of the poloidal magnetic field returns to the polarity of the initial condition; (iii) the equatorward migration of longitudinal field structures during these cycles; (iv) the poleward migration of oppositely-signed flux; and (v) a "grand minimum," where there is a period of relative magnetic quiescence at low-latitudes and disrupted polarity cycles after which the previous polarity cycle is recovered. These aspects bear resemblance to some of the behavior of solar magnetism. It, however, does possess different time scales. Further, it does not have explicit surface flux emergence, and there is a significant modulation of the differential rotation.

The most prevalent properties of K3S involve both a prominent solar-like differential rotation and distinctive wreaths of magnetism. Similar properties have been realized in a broad range of simulations carried out previously with ASH (e.g., Brown et al. 2010, 2011; Augustson et al. 2013; Nelson et al. 2013a). The primary characteristic shared among these simulations is that they typically have a low Rossby number, leading to the formation of large-scale toroidal magnetic wreaths. Another common feature in global-scale convective dynamo simulations is that the interplay between the mean toroidal magnetic field and the angular velocity leads to a significant modulation of the differential rotation. In K3S this contributes to the waxing and waning of the magnetic energy since the production of mean toroidal magnetic energy relies upon the shear of the differential rotation though the Ω effect. In particular, as the shear reaches a minimum due to the Lorentz forces, the magnetic fields subsequently weaken. Yet once the magnetic fields are sufficiently diminished, the convective patterns at low latitudes regain structures that can more efficiently regenerate the differential rotation. Thus the magnetic field generation starts anew. The strong feedback of the Lorentz forces on the differential rotation leads to the equatorward propagation of the magnetic fields. As the wreaths approach the equator, there is an increase in the cross-equatorial magnetic flux that permits the low latitude convection to generate poloidal magnetic fields with the opposite polarity of the dominant magnetic wreaths. This oppositely-signed magnetic flux is then advected and diffused, eventually reaching

the poles and completing a magnetic polarity reversal. This dynamo regime is distinct from mean-field models of cyclic dynamos that do not involve Lorentz-force feedbacks, and in some ways it operates in contrast to typical flux-transport dynamos. Such robust properties appear to be unaffected by the new SLD treatment for diffusion of vorticity. What SLD admits are noticeably lower magnetic Prandtl numbers Pm, which allow a richer suite of temporal variability. The lower Pm, combined with a strong stratification, has resulted in K3S possessing more regular cycles and reversals than obtained in previous wreath-building ASH simulations.

The substantial advances in supercomputing capabilities has led to the recent development of a series of global-scale 3-D MHD simulations that all possess the interplay of convection, rotation, and magnetism. The K3S simulation builds upon this contemporary work (e.g., Ghizaru et al. 2010; Brown et al. 2010; Racine et al. 2011; Brown et al. 2011; Käpylä et al. 2012; Augustson et al. 2013; Nelson et al. 2013a; Fan & Fang 2014). The two common threads in those studies is the generation of large-scale coherent magnetic wreaths within the convection zone and the presence of a solar-like differential rotation achieved due to the low Rossby number of the convective flows. Some of those simulations exhibit regular magnetic polarity reversals. Indeed, both K3S and the Millennium simulation (Charbonneau 2014), which also includes a tachocline at the base of the convection zone, have attained many such reversals over an extended interval. Furthermore, K3S and the Millennium simulation both show that the amplitude of the magnetic cycles appears to be regulated by the feedback of the Lorentz forces on the differential rotation (Racine et al. 2011). They do, however, appear to operate differently in the context of mean-field theory. Namely, the Millennium simulation seems to be akin to an α^2-Ω dynamo (Racine et al. 2011), whereas in K3S the α effect generating toroidal magnetic fields is quite weak leading it to be more similar to the classical α-Ω dynamo. In a smaller subset of those simulations including K3S, equatorward propagation of the large-scale magnetic structures is another shared feature during their magnetic cycles. In the simulations of Käpylä et al. (2013) and Warnecke et al. (2014), a sufficiently large density stratification and the linear dynamo waves of mean-field theory appear to provide an explanation for the equatorward propagation of the magnetic fields. Similarly, K3S shares a large density stratification. However, unlike a kinematic α-Ω dynamo, the equatorward propagation arises from the nonlinear interaction of the magnetic fields and the differential rotation.

The K3S simulation exhibits an interval of 16 years during which the magnetic cycles are disrupted and the magnetic energy is reduced at low latitudes, after which the regular cycles resume. This is somewhat reminiscent of solar grand minima, when the observed solar magnetic energy is substantially reduced and sunspot emergence is largely interrupted (e.g., Ribes & Nesme-Ribes 1993; McCracken 2007). As such, the disruption of regular cycling in K3S has been loosely identified as a grand minimum, since this is the first appearance of such long-sought behavior in a 3-D global-scale simulation. The likely mechanism that leads to intermittency such as this grand minimum in K3S is the interplay of symmetric and antisymmetric dynamo families. During the typical magnetic energy cycles, the antisymmetric dynamo family is dominant throughout the majority of the cycle in which the magnitude of the odd-ordered modes of the poloidal magnetic field is much larger than those of the even-ordered modes. In contrast during the grand minimum, the even modes can be equal to, and at times greater than, the magnitude of the odd modes. The increased symmetry about the equator of the poloidal field disrupted the ability of the dynamo to fully reverse the antisymmetric modes and led to a weaker dynamo state during the grand minimum, in which the low-latitude volume-integrated magnetic energy decreased by about 50%.

What is particularly striking is that during the magnetic energy cycle preceding the grand minimum, magnetic structures in the northern and the southern hemispheres become highly asynchronous, leading to the strong excitation of many symmetric modes in the poloidal magnetic field. It also appears that the typical phasing of the magnetic field between the deep convection zone (CZ) and that of the upper CZ is disrupted. Together those losses of phase coherence admit dynamo action from both the symmetric and the antisymmetric modes, which heralds the entrance of the grand minimum. Eventually, the symmetric modes decay in amplitude, allowing the antisymmetric family and thus the dipole mode to reassert its dominance. In earlier studies of simpler though nonlinear mean-field dynamo models, there is a clear variability between the dominance of antisymmetric or symmetric dynamo modes in those models (e.g., Tobias 1997; Moss & Brooke 2000; Brooke et al. 2002; Bushby 2006). Such variability can lead to intervals of deep minima. Moreover, it was seen that the interplay between the dynamo families is critical to achieve intermittent and aperiodic dynamo states. Those studies have further shown that low magnetic Prandtl numbers favor solutions with extended intervals of minimal activity. This provides some background for how the lower Pm achieved with the SLD treatment in K3S may lead to the appearance of deep minima and the coupling of the symmetric and antisymmetric dynamo families.

Though the K3S simulation does share robust features with other global-scale convective dynamos, it must be stated that the results do depend on the dissipation through the effective values of the Reynolds and magnetic Reynolds numbers, Re and Rm. Yet there are currently no global convective dynamo simulations in the known literature that demonstrate convergence with increasing Re and Rm. Since the SLD diffusion is linked with the spatial resolution, this sensitivity to Re and Rm translates to a dependence on resolution. Particularly, reducing the effective viscous diffusion using the SLD method likely permitted this solution to enter an interesting parameter regime. Further simulations are being carried out to characterize parameter sensitivities, including the identification of the factors that set the cycle period and the search for asymptotic behavior. These results will be presented in future papers. The SLD method has been shown to converge for solar surface magnetoconvection simulations (Rempel 2012), but large-scale dynamos may be more subtle. Nevertheless, the K3S simulation lies in an interesting parameter regime that exhibits a novel, self-consistent, cyclic convective dynamo with intermittent cycle modulation that may share some dynamic features with dynamos in more extreme parameter regimes and indeed, in stars.

Despite rotating three times faster than the Sun and parameterizing large portions of its vast range of scales, some of the features of the dynamo that may be active within the Sun's interior have been realized in this global-scale ASH simulation. For instance, the period of the magnetic polarity cycle in K3S is 6.2 years. This period is about 243 times the rotation period, which can be compared to the Sun's ratio of about 287. Under a linear scaling of the rotation rate, a comparable solar simula-

tion could have a half-period of 9.3 years, close to the sunspot cycle period of the Sun. So, although this model star rotates more rapidly than the Sun and has a shorter cycle period, the ratio of the cycle period to the rotation period is not much different. Particularly, its rapid rotation helped to put it into an interesting Rossby number regime that permits a solar-like differential rotation (fast equator, slow poles), and once there it produced a cycle period that may be non-dimensionally comparable to that of the Sun. Indeed, the increasingly frequent emergence of 3-D convective dynamo simulations that exhibit solar-like dynamo features such as this one are reshaping the understanding of the physics of convective dynamos. Thus, future global-scale dynamo simulations promise new insights into solar and stellar dynamos as supercomputing resources continue to advance.

ACKNOWLEDGMENTS

The authors wish to thank an anonymous referee for extensive and helpful comments. A singular thanks is due to Nicholas Featherstone for his effort in greatly improving the computational efficiency and scaling of the ASH code. The authors also thank Bradley Hindman, Mark Rast, Matthias Rempel, and Regner Trampedach for useful conversations. This research was supported by NASA through the Heliophysics Theory Program grant NNX11AJ36G, with additional support for Augustson first through the NASA NESSF program by award NNX10AM74H and second through the NCAR Advanced Study Program. NCAR is supported by the NSF. A.S. Brun acknowledges financial support through ANR TOUPIES, CNES Solar Orbiter grant and INSU/PNST. The computations were primarily carried out on Pleiades at NASA Ames with SMD grants g26133 and s0943, and also used XSEDE resources for analysis. This work further utilized the Janus supercomputer, which is supported by the NSF award CNS-0821794 and the University of Colorado Boulder.

REFERENCES

Augustson, K. C., Brown, B. P., Brun, A. S., Miesch, M. S., & Toomre, J. 2012, ApJ, 756, 169
Augustson, K. C., Brun, A. S., Miesch, M. S., & Toomre, J. 2014, Cool Stars 18 Electronic Proc., 1, 437
Augustson, K. C., Brun, A. S., & Toomre, J. 2013, ApJ, 777, 153
Babcock, H. W. 1961, ApJ, 133, 572
Baliunas, S. L., Nesme-Ribes, E., Sokoloff, D., & Soon, W. H. 1996, ApJ, 460, 848
Barnes, S. A. 2007, ApJ, 669, 1167
Beer, J., Tobias, S., & Weiss, N. 1998, Solar Phys., 181, 237
Benevolenskaya, E. E. 2004, A&A, 428, L5
Borges, R., Carmona, M., Costa, B., & Don, W. S. 2008, J. Comp. Phys., 227, 3191
Brandenburg, A. 2009, ApJ, 697, 1206
Brandenburg, A., & Spiegel, E. A. 2008, Astro. Nachr., 329, 351
Brandenburg, A., & Subramanian, K. 2005, Phys. Rep., 417, 1
Brooke, J., Moss, D., & Phillips, A. 2002, A&A, 395, 1013
Brown, B. P., Browning, M. K., Brun, A. S., Miesch, M. S., & Toomre, J. 2008, ApJ, 689, 1354
—. 2010, ApJ, 711, 424
Brown, B. P., Miesch, M. S., Browning, M. K., Brun, A. S., & Toomre, J. 2011, ApJ, 731, 69
Browning, M. K. 2008, ApJ, 676, 1262
Browning, M. K., Miesch, M. S., Brun, A. S., & Toomre, J. 2006, ApJ, 648, L157
Brun, A. S., Garcia, R. A., Houdek, G., Nandy, D., & Pinsonneault, M. 2014, Space Sci. Rev., 1, 1
Brun, A. S., Miesch, M. S., & Toomre, J. 2004, ApJ, 614, 1073
Bushby, P. J. 2006, MNRAS, 371, 772
Charbonneau, P. 2010, Liv. Rev. Sol. Phys., 7, 3
—. 2013, J. Phys. Conf. Ser., 440, 012014
—. 2014, ARA&A, 52, 251
Charbonneau, P., St-Jean, C., & Zacharias, P. 2005, ApJ, 619, 613
Christensen-Dalsgaard, J., Dappen, W., Ajukov, S. V., et al. 1996, Science, 272, 1286
Clune, T. L., Elliott, J. R., Miesch, M. S., Toomre, J., & Glatzmaier, G. A. 1999, Para. Comp., 25, 361
Cossette, J.-F., Charbonneau, P., & Smolarkiewicz, P. K. 2013, ApJ, 777, L29
DeRosa, M. L., Brun, A. S., & Hoeksema, J. T. 2012, ApJ, 757, 96
Eddy, J. A. 1976, Science, 192, 1189
Fan, Y., & Fang, F. 2014, ApJ, 789, 35
Fan, Y., Featherstone, N., & Fang, F. 2013, ArXiv e-prints
Fares, R., Moutou, C., Donati, J.-F., et al. 2013, MNRAS
Favata, F., Micela, G., Orlando, S., et al. 2008, A&A, 490, 1121
Gallet, B., & Pétrélis, F. 2009, Phys. Rev. E, 80, 035302
Ghizaru, M., Charbonneau, P., & Smolarkiewicz, P. K. 2010, ApJ, 715, L133
Gilman, P. A. 1983, ApJS, 53, 243
Glatzmaier, G. A. 1985, ApJ, 291, 300
Gleissberg, W. 1939, The Observatory, 62, 158
Gruzinov, A. V., & Diamond, P. H. 1994, Phys. Rev. Lett., 72, 1651
Guerrero, G., Smolarkiewicz, P. K., Kosovichev, A. G., & Mansour, N. N. 2013, ApJ, 779, 176
Hathaway, D. H. 2010, Liv. Rev. Sol. Phys., 7, 1
Hempelmann, A., Schmitt, J. H. M. M., & Stępień, K. 1996, A&A, 305, 284
Jiang, G. 1996, J. Comp. Phys., 126, 202
Jouve, L., Brown, B. P., & Brun, A. S. 2010, A&A, 509, A32
Käpylä, P. J., Korpi, M. J., Ossendrijver, M., & Stix, M. 2006, A&A, 455, 401
Käpylä, P. J., Mantere, M. J., & Brandenburg, A. 2011a, Astro. Nachr., 332, 883
—. 2012, ApJ, 755, L22
Käpylä, P. J., Mantere, M. J., Cole, E., Warnecke, J., & Brandenburg, A. 2013, ApJ, 778, 41
Käpylä, P. J., Mantere, M. J., Guerrero, G., Brandenburg, A., & Chatterjee, P. 2011b, A&A, 531, A162
Karak, B. B., & Choudhuri, A. R. 2013, Res. Astron. Astrophys., 13, 1339
Krause, F., & Raedler, K.-H. 1980, Mean-field magnetohydrodynamics and dynamo theory
Malkus, W. V. R., & Proctor, M. R. E. 1975, J. Fluid Mech., 67, 417
Malyshkin, L. M., & Boldyrev, S. 2010, Phys. Rev. Lett., 105, 215002
Mathur, S., García, R. A., Morgenthaler, A., et al. 2013, A&A, 550, A32
Matt, S. P., Brun, A. S., Baraffe, I., Bouvier, J., & Chabrier, G. 2015, ApJ, 799, L23
McCracken, K. G. 2007, J. Geophys. Res. (Space Physics), 112, 9106
McIntyre, M. E. 1998, Progress of Theoretical Physics Supplement, 130, 137
Metcalfe, T. S., Basu, S., Henry, T. J., et al. 2010, ApJ, 723, L213
Miesch, M. S., & Brown, B. P. 2012, ApJ, 746, L26
Miesch, M. S., Elliott, J. R., Toomre, J., et al. 2000, ApJ, 532, 593
Miesch, M. S., & Hindman, B. W. 2011, ApJ, 743, 79
Mignone, A., Tzeferacos, P., & Bodo, G. 2010, J. Comp. Phys., 229, 5896
Moffatt, H. K. 1978, Magnetic field generation in electrically conducting fluids
Morgenthaler, A., Petit, P., Morin, J., et al. 2011, Astro. Nachr., 332, 866
Moss, D., & Brooke, J. 2000, MNRAS, 315, 521
Nelson, N. J., Brown, B. P., Brun, A. S., Miesch, M. S., & Toomre, J. 2013a, ApJ, 762, 73
Nelson, N. J., Brown, B. P., Sacha Brun, A., Miesch, M. S., & Toomre, J. 2013b, Sol. Phys., 20
Nishikawa, N., & Kusano, K. 2008, Physics of Plasmas, 15, 082903
Parker, E. N. 1955, ApJ, 122, 293
—. 1977, ARA&A, 15, 45
—. 1987, ApJ, 312, 868
Passos, D., & Charbonneau, P. 2014, A&A, 568, A113
Ponty, Y., Mininni, P. D., Montgomery, D. C., et al. 2005, Phys. Rev. Lett., 94, 164502
Pouquet, A., Frisch, U., & Leorat, J. 1976, J. Fluid Mech., 77, 321
Racine, É., Charbonneau, P., Ghizaru, M., Bouchat, A., & Smolarkiewicz, P. K. 2011, ApJ, 735, 46
Rempel, M. 2012, ApJ, 750, 62
Rempel, M., Schüssler, M., & Knölker, M. 2009, ApJ, 691, 640
Ribes, J. C., & Nesme-Ribes, E. 1993, A&A, 276, 549
Saar, S. H. 2009, in Astro. Soc. Pac. Conf. Ser., Vol. 416, Solar-Stellar Dynamos as Revealed by Helio- and Asteroseismology: GONG 2008/SOHO 21, 375
Schekochihin, A. A., Iskakov, A. B., Cowley, S. C., et al. 2007, New J. Phys., 9, 300
Simard, C., Charbonneau, P., & Bouchat, A. 2013, ApJ, 768, 16
Steenbeck, M., & Krause, F. 1969, Astro. Nachr., 291, 49
Steenbeck, M., Krause, F., & Rädler, K.-H. 1966, Zeit. Natur. Teil A, 21, 369
Strugarek, A., Brun, A. S., Mathis, S., & Sarazin, Y. 2013, ApJ, 764, 189
Suresh, A., & Huynh, H. T. 1997, J. Comp. Phys., 136, 83
Tobias, S. M. 1997, A&A, 322, 1007
Usoskin, I. G. 2013, Liv. Rev. Sol. Phys., 10, 1
Čada, M., & Torrilhon, M. 2009, J. Comp. Phys., 228, 4118
Warnecke, J., Käpylä, P. J., Käpylä, M. J., & Brandenburg, A. 2014, ApJ, 796, L12
Yoshimura, H. 1975, ApJ, 201, 740

APPENDIX

A. SLOPE-LIMITED DIFFUSION IN ASH

There are currently three methods for stabilizing the numerics in ASH, which like all spectral codes is inherently unstable without a sufficient level of explicit diffusion. The first is that described in §2 with a renormalization of the molecular diffusion coefficients into eddy coefficients, the second is the spectral extrapolation method as in the dynamic Smagorinski method (Nelson et al. 2013a), and most recently the numerically stabilizing slope-limited diffusion (SLD) scheme. SLD has many possible formulations, with the one employed in ASH being similar to that found in Rempel et al. (2009) and Fan et al. (2013). At its heart, the SLD method attempts to push the solution toward a state that is monotonically smooth.

In ASH, a smoothed solution is obtained through the following steps: a slope-limited piecewise linear approximation to the solution is constructed; the difference between the left and right reconstructed values at a cell edge is computed; this difference is then multiplied by a diffusive rate to create a diffusive flux at the cell edge; finally, the divergence of this flux is computed and added to the solution. Since this diffusion is nonlinear and a finite-volume based scheme, it is computed in physical space and so must be transformed into spectral space before being added to the other nonlinear terms advanced with an Adams-Bashforth time-stepping scheme.

Because of the converging longitudinal grid near the poles in physical space configuration of ASH, the SLD is filtered in longitude. This is accomplished through two processes. First the full grid-wise SLD is computed; a second SLD is computed with a continuously increasing cell size as the poles are approached, which incorporates a greater number of points in a given cell. The cell size increases as $\csc\theta$, with the requirement that there be no fewer than eight SLD cells at high latitudes. The slope is reconstructed over the larger cell such that the individual points within the cell see the same slope in the cell. These two diffusive fields are weighted with $\sin^2\theta$ for the first field and by $\cos^2\theta$ for the second field. This allows for a more uniform resolution of the SLD operator over the nonuniform griding of the sphere.

A.1. *Constructing a Slope-Limited Diffusion*

A piecewise reconstruction of values at the cell edge that are concurrent with the cell center value takes the general form of a Taylor series as

$$q_{i+1/2} = q_i + \sum_{k=1} \left(x_{i+1/2} - x_i\right)^k \left.\frac{\widetilde{\Delta^k q}}{\Delta x^k}\right|_i , \tag{A1}$$

where each order of the numerical derivative is limited in some fashion to maintain monotonicity as is indicated with the tilde. There are a few techniques for computing these higher-order derivatives and their limited values, but they become increasingly complex with each increasing order of polynomial approximation (e.g., Jiang 1996; Suresh & Huynh 1997; Borges et al. 2008; Čada & Torrilhon 2009; Mignone et al. 2010). The most well studied schemes are linear reconstructions, which will suffice for creating a diffusive operator.

The piecewise linear reconstruction at the cell edges requires at least three derivative values and three quantity values at adjacent cell centers of a given quantity q in a particular direction. Each direction is treated equally, so the following will focus only on one of them; call it coordinate x with index i. First define the cell-edge derivative approximation as

$$\left.\frac{\partial q}{\partial x}\right|_{i+1/2} = \frac{1}{2}\left[\left.\frac{\partial q}{\partial x}\right|_{i+1} + \left.\frac{\partial q}{\partial x}\right|_{i}\right] \tag{A2}$$

Next define the the average cell-centered derivative with

$$\left\langle \left.\frac{\partial q}{\partial x}\right|_i \right\rangle = \frac{1}{2 + w_{i+1} + w_{i-1}} \left[w_{i+1} \left(\left.\frac{\partial q}{\partial x}\right|_{i+1} + \left.\frac{\partial q}{\partial x}\right|_{i} \right) + w_{i-1} \left(\left.\frac{\partial q}{\partial x}\right|_{i} + \left.\frac{\partial q}{\partial x}\right|_{i-1} \right) \right] . \tag{A3}$$

where the weights w are $w_{i-1} = \text{minmod}\left[q_i, q_{i-1}\right]$ and $w_{i+1} = \text{minmod}\left[q_i, q_{i+1}\right]$, and

$$\text{minmod}\left[x, y\right] = \begin{cases} \min\left[1, \frac{x}{y}\right] & \text{for} \, xy > 0 \\ 0 & \text{otherwise} \end{cases} . \tag{A4}$$

Such a weighting minimizes the overshoot and undershoot of the solution near a discontinuity, allowing greater monotonicity. Let the slope-limiting function be defined so that

$$\psi_i = \psi \left[\left\langle \left.\frac{\partial q}{\partial x}\right|_i \right\rangle \left(\left.\frac{\partial q}{\partial x}\right|_i \right)^{-1} \right] \tag{A5}$$

and bounded so that $0 \leq \psi_i \leq 1$. The limited slope at cell center is then constructed as

$$\left.\widetilde{\frac{\partial q}{\partial x}}\right|_i = (1-\psi_i)\left\langle \left.\frac{\partial q}{\partial x}\right|_i \right\rangle + \psi_i \left.\frac{\partial q}{\partial x}\right|_i \tag{A6}$$

Thus the cell-edge difference is $\delta q_{i+1/2} = q^R_{i+1/2} - q^L_{i+1/2}$, or

$$\delta q_{i+1/2} = \Delta q_{i+1/2} - \frac{1}{2}\left[\Delta x_{i+1}\left.\widetilde{\frac{\partial u}{\partial x}}\right|_{i+1} + \Delta x_i \left.\widetilde{\frac{\partial u}{\partial x}}\right|_i\right], \tag{A7}$$

where the slope-limited, linearly reconstructed values of q on the left and right sides of a cell edge are $q^L_{i+1/2}$ and $q^R_{i+1/2}$, $\Delta q_{i+1/2} = q_{i+1} - q_i$, and $\Delta x_i = x_i - x_{i-1}$. In this case, the diffusive flux is then controlled with a coefficient that sets the rate at which the solution achieves a state that is linearly smooth and monotonic. The diffusive flux in direction x at the cell edge is then $F^x_{i+1/2} = c_{i+1/2}\delta q_{i+1/2}$ with the diffusion speed at the cell edge defined as

$$c_{i+1/2} = \beta\left(\delta q_{i+1/2}, \Delta q_{i+1/2}; \alpha\right)\sqrt{\mathrm{v}^2_{\min} + \mathbf{v}'^2_{i+1/2}}. \tag{A8}$$

Here $\mathrm{v}_{\min}$ is a minimum speed that sets the base level of diffusion, and the fluctuating velocities locally enhance it. The function β further isolates the diffusion to regions of the largest discontinuities and prevents anti-diffusion. It is defined as $\beta\left(\delta q_{i+1/2}, \Delta q_{i+1/2}; \alpha\right) = \left(\mathrm{minmod}\left[\delta q_{i+1/2}, \Delta q_{i+1/2}\right]\right)^\alpha$, with α some positive value. Now, let r_i be the cell center in radius of a grid cell, θ_j the center in colatitude, and φ_k the center in longitude. Following the definition of finite volumes, the rate of change induced in the quantity q through the diffusive flux in spherical coordinates is

$$\begin{aligned}\left.\frac{\partial q}{\partial t}\right|_{\mathrm{SLD}} = \frac{3}{2}\frac{r^2_{i+1/2} - r^2_{i-1/2}}{r^3_{i+1/2} - r^3_{i-1/2}}\Bigg[&2\frac{r^2_{i+1/2}F^r_{i+1/2} - r^2_{i-1/2}F^r_{i-1/2}}{r^2_{i+1/2} - r^2_{i-1/2}} \\ &+ \frac{\sin\theta_{j+1/2}F^\theta_{j+1/2} - \sin\theta_{j-1/2}F^\theta_{j-1/2}}{\cos\theta_{j-1/2} - \cos\theta_{j+1/2}} \\ &+ \frac{\theta_{j+1/2} - \theta_{j-1/2}}{\cos\theta_{j-1/2} - \cos\theta_{j+1/2}}\frac{F^\varphi_{k+1/2} - F^\varphi_{k-1/2}}{\varphi_{k+1/2} - \varphi_{k-1/2}}\Bigg],\end{aligned} \tag{A9}$$

where unchanging indices have been suppressed.

In order to conserve energy in the domain, the diffusive and dissipative processes must be accounted for. Since the entropy diffusion is automatically energy conserving, only the dissipative exchange of energy from the velocity fields to the entropy field need be examined. With this in mind, the viscous component of the entropy production due to SLD is

$$\overline{\rho}\,\overline{T}\left.\frac{\partial s}{\partial t}\right|_{\mathrm{SLD}} = \left.\frac{\partial}{\partial t}\left(\frac{1}{2}\overline{\rho}\mathbf{v}^2\right)\right|_{\mathrm{SLD}} - \overline{\rho}\mathbf{v}\cdot\left.\frac{\partial \mathbf{v}}{\partial t}\right|_{\mathrm{SLD}}, \tag{A10}$$

where $\overline{\rho}$ and $\overline{T}$ are the background density and temperature in an ASH simulation. Basically it is the difference between the diffusion of the kinetic energy and the energy difference arising from the diffusion of the velocity field (e.g. $\nabla\cdot\mathbf{F}_{\mathrm{ke}} - \overline{\rho}\mathbf{v}\cdot\nabla\cdot\mathcal{F}_{\mathbf{v}}$).

A.2. *Mathematical Implications of SLD*

Since this diffusion scheme is derived from finite volumes, it is conservative to within machine precision, with the adage "one cell's loss is another's gain" holding here. It is useful to show that this diffusion reduces to a Laplacian diffusion under certain assumptions. Assume first that the diffusion speed is set to the constant $c = v_{\min}$. Second, let the function $\beta = 1$ and further let there be no discontinuities in the domain (so that the weights w are all unity). For simplicity, also assume a uniform mesh in one dimension, thus the divergence of the total diffusive flux is

$$\begin{aligned}\boldsymbol{\nabla}\cdot\mathbf{F} &= \frac{c}{\Delta x}\left(\delta q_{i+1/2} - \delta q_{i-1/2}\right), \\ &= c\Delta x\left(\frac{q_{i+1} - 2q_i + q_{i-1}}{\Delta x^2} - \frac{1}{2\Delta x}\left[\left.\widetilde{\frac{\partial u}{\partial x}}\right|_{i+1} - \left.\widetilde{\frac{\partial u}{\partial x}}\right|_{i-1}\right]\right).\end{aligned} \tag{A11}$$

Notice that the first term is just the second-order approximation to the second derivative, whereas the second is the slope-limited approximation to the second derivative. So, this operator may be Taylor expanded to see that

$$\boldsymbol{\nabla}\cdot\mathbf{F} = c\Delta x\left[\frac{\partial^2 q}{\partial x^2} - \widetilde{\frac{\partial^2 q}{\partial x^2}} + \mathcal{O}\left(\Delta x^2\right)\right]_i. \tag{A12}$$

Equation (A12) elucidates the first-order behavior of the slope-limited diffusion operator. The difference between the unfiltered and the filtered Laplacian operators reduces the overall diffusion by subtracting off a smoothed Laplacian, which is by construction always less oscillatory than the local Laplacian. This leaves only the local fluctuations to be diffused away with the coefficient $c\Delta x$. The higher-order components yield a filtered hyper-diffusivity.

A.3. *Estimated Fluid Parameters*

As a point of reference, and given the values of the eddy diffusivities presented in §2, a few standard fluid parameters can be estimated. The first is an effective fluid Reynolds number $\mathrm{Re} = u_{\mathrm{rms}} d/\nu_{\mathrm{eff}}$. The length-scale d is taken to be the depth of the convection zone (175 Mm), and the rms velocity near the upper boundary is measured to be $100\,\mathrm{m\,s^{-1}}$. Given the argument in Appendix A.2, the effective diffusion coefficient could be estimated to be $\nu_{\mathrm{eff}} \approx c\Delta x \approx 1.75\times10^{13}\mathrm{cm^2\,s^{-1}}$ at the upper boundary, where c is the diffusion advection speed. Yet this is not a complete estimate though, as the strength of the SLD operator's damping depends upon the local value of the velocity gradient. This spatial dependence is largely governed by the morphology of resolved flows. As discussed in A.2, the SLD diffusion operator can become akin to a diffusion coefficient multiplied by the difference of a grid-level Laplacian and a filtered Laplacian. Thus, the average value of $|\nabla^2\mathbf{v} - \widetilde{\nabla}^2\mathbf{v}|$ needs to be estimated to better approximate the SLD diffusion coefficient. The radial gradient of the flows is fairly small when compared to the horizontal gradients as the convective cells tend to stretch across the convection zone. Further, within the relatively laminar conditions of an upflow, this difference is again small and so the contribution of the upflows can be neglected. Hence,

$$\begin{aligned}\left\langle\left|\nabla^2\mathbf{v} - \widetilde{\nabla}^2\mathbf{v}\right|\right\rangle &\approx \frac{A_{\mathrm{d}}}{A}\left(\frac{u_{\mathrm{rms}}}{\Delta x^2} - \frac{u_{\mathrm{rms}}}{\ell^2}\right) \approx \frac{A_{\mathrm{d}}}{A}\left(1 - \frac{\Delta x^2}{\ell^2}\right)\frac{u_{\mathrm{rms}}}{\Delta x^2} \\ \Rightarrow c\Delta x\left(\nabla^2\mathbf{v} - \widetilde{\nabla}^2\mathbf{v}\right) &\approx c\Delta x\frac{A_{\mathrm{d}}}{A}\nabla^2\mathbf{v}\end{aligned}$$

where A is the total surface area, A_{d} is the area occupied by steep gradients at the edges of a downflow, Δx is an average grid spacing, and ℓ is the filter length scale.

The effective SLD diffusion coefficient can thus be quantified as $\nu_{\mathrm{eff}} = c\Delta x A_{\mathrm{d}}/A$. This leaves the task of estimating the effective diffusion profile of the downflows. In this simulation they are primarily composed of two regions, the downflow core and the steep transition zones between the core and the surrounding upflows as might be deduced from Figures 4(b)-(f). Those transition zones are where the velocity gradient is largest and they occupy approximately one-third of the horizontal area of a downflow, whereas the downflows themselves cover roughly one-third of the total surface area. Therefore, the effective diffusion coefficient at the upper boundary is $2\times10^{12}\mathrm{cm^2\,s^{-1}}$. As with the Newtonian diffusion coefficients for the thermal and magnetic fields, the value c follows a $\overline{\rho}^{-1/2}$ profile. Thus, ν_{eff} is reduced by a factor of four at mid-convection zone, yielding an effective Reynolds number of $\mathrm{Re}_{\mathrm{eff}} \approx 350$ there.

B. EVOLUTION OF DIFFERENTIAL ROTATION KINETIC ENERGY

The derivation of the equation for the time evolution of the volume-integrated energy contained in the differential rotation, as assessed in §4.2, involves some subtlety in the role of the boundary terms. First, note that the evolution of the mean specific angular momentum can be written as the divergence of a flux as $\partial_t\langle L\rangle = -\boldsymbol{\nabla}\cdot\langle\mathbf{F}_L\rangle$, where for the anelastic system $\langle L\rangle = \overline{\rho}\lambda\langle \mathrm{v}_\varphi\rangle$ and where the angular momentum fluxes $\langle\mathbf{F}_L\rangle$ are specified below. Thus, $\langle\Omega\rangle\partial_t\langle L\rangle = 1/2\partial_t\overline{\rho}\langle \mathrm{v}_\varphi\rangle^2$. Next, multiply the evolution equation by the angular velocity $\langle\Omega\rangle$ and apply the chain rule for the divergence operator as $\langle\Omega\rangle\boldsymbol{\nabla}\cdot\langle\mathbf{F}_L\rangle = \boldsymbol{\nabla}\cdot(\langle\Omega\rangle\langle\mathbf{F}_L\rangle) - \langle\mathbf{F}_L\rangle\cdot\boldsymbol{\nabla}\langle\Omega\rangle$ to see that

$$\frac{\partial}{\partial t}\frac{1}{2}\overline{\rho}\langle \mathrm{v}_\varphi\rangle^2 = \langle\mathbf{F}_L\rangle\cdot\boldsymbol{\nabla}\langle\Omega\rangle - \boldsymbol{\nabla}\cdot\left(\langle\Omega\rangle\langle\mathbf{F}_L\rangle\right), \tag{B1}$$

with $\langle\mathbf{F}_L\rangle = \overline{\rho}\lambda\langle \mathrm{v}_\varphi\mathbf{v}\rangle - \lambda\langle\mathcal{D}\rangle\cdot\hat{\boldsymbol{\varphi}} - \lambda\langle B_\varphi\mathbf{B}\rangle/4\pi$, where $\mathcal{D}$ is the viscous diffusion tensor. Since the viscous eddy diffusivity is very small in this simulation, and the slope-limited diffusion provides an especially small level of diffusion to the smooth mean fields, this term is neglected. Hence, when integrated over the volume of the domain and applying Gauss's theorem to the complete divergence term, the evolution of the total energy contained in the differential rotation can be written as

$$\begin{aligned}K_\varphi(t) &= \int_V dV\frac{\partial}{\partial t}\frac{1}{2}\overline{\rho}\langle \mathrm{v}_\varphi\rangle^2 = \int_V dV\lambda\left[\overline{\rho}\langle \mathrm{v}_\varphi\mathbf{v}\rangle - \frac{\langle B_\varphi\mathbf{B}\rangle}{4\pi}\right]\cdot\boldsymbol{\nabla}\langle\Omega\rangle \\ &- \int_S dS\langle\Omega\rangle\left[\overline{\rho}\lambda\langle \mathrm{v_r v}_\varphi\rangle - \frac{\langle\lambda B_\varphi B_{\mathrm{r}}\rangle}{4\pi}\right] = K_\varphi^V(t) + K_\varphi^S(t),\end{aligned} \tag{B2}$$

where the properties of the full spherical geometry are leveraged so that only radial boundaries can in principle contribute to the evolution of the system. In the above integral, S is the union of the spherical surfaces at the upper and lower radial boundaries. However, the impenetrability of the radial boundaries requires that the first term in the surface integral be zero. Similarly, the perfectly conducting condition at the lower boundary requires that $B_{\mathrm{r}} = 0$ there, so the second term also vanishes at the lower boundary. In contrast, the upper boundary is a potential field condition, meaning that the magnetic flux term may not necessarily vanish there. However, this value can be shown to be zero with the equations utilized in ASH. Given that $\mathbf{B}$ is a solenoidal field, one can define $\mathbf{B} = \boldsymbol{\nabla}\times\boldsymbol{\nabla}\times C\hat{\mathbf{r}} + \boldsymbol{\nabla}\times A\hat{\mathbf{r}}$, with two scalar fields $C = C(t,r,\theta,\varphi)$ and $A = A(t,r,\theta,\varphi)$. Therefore at the upper boundary where $r = r_2$, it can be seen that $B_{\mathrm{r}} = -\nabla_H^2 C$ and $\lambda B_\varphi = \partial_{\varphi,\mathrm{r}}C - \sin\theta\partial_\theta A$, with ∇_H^2 the Laplacian on spherical surfaces. Therefore, $B_{\mathrm{r}} = \sum_{\ell,\mathrm{m}}\ell(\ell+1)C_\ell^{\mathrm{m}}Y_\ell^{\mathrm{m}}/r_2^2$, where $Y_\ell^{\mathrm{m}} = N_\ell^{\mathrm{m}}P_\ell^{\mathrm{m}}(\theta)\exp(im\varphi)$ are spherical harmonics, the N_ℓ^{m} the spherical harmonic normalization coefficient, the P_ℓ^{m} are associated Legendre polynomials, and the $C_\ell^{\mathrm{m}} = C_\ell^{\mathrm{m}}(r_2)$ are the spherical harmonic expansion coefficients of the vector potential component C. The potential field boundary condition at $r = r_2$ implies that $\partial_r C_\ell^{\mathrm{m}} = -\ell C_\ell^{\mathrm{m}}/r_2$ and $A = 0$, so at $r = r_2$ the following holds $\lambda B_\varphi = -\sum_{\ell,\mathrm{m}} im\ell C_\ell^{\mathrm{m}}Y_\ell^{\mathrm{m}}/r_2$. Thus, the surface integral in Equation (B2) becomes

$$K_\varphi^S(t) = \int_S dS\langle\Omega\rangle \frac{\langle\lambda B_\varphi B_r\rangle}{4\pi} = \int_S \frac{dS}{16\pi^3 r_2^3} \sum_{\ell_1,\mathrm{m}_1} \left[\tilde{\Omega}_{\ell_1} \int_0^{2\pi} d\varphi' Y_{\ell_1}^{\mathrm{m}_1}\right]$$
$$\times \sum_{\substack{\ell_2,\ell_3,\\ \mathrm{m}_2,\mathrm{m}_3}} \left[-i\mathrm{m}_2\ell_2\ell_3(\ell_3+1) C_{\ell_2}^{\mathrm{m}_2} C_{\ell_3}^{\mathrm{m}_3} \int_0^{2\pi} d\varphi' Y_{\ell_2}^{\mathrm{m}_2} Y_{\ell_3}^{\mathrm{m}_3}\right], \tag{B3}$$

where $\tilde{\Omega}_\ell$ are the coefficients of the spherical harmonics expansion of the axisymmetric differential rotation. The integrals over φ' require that $\mathrm{m}_1 = 0$ and $\mathrm{m}_2 + \mathrm{m}_3 = 0$, leaving

$$K_\varphi^S(t) = \frac{-i}{2r_2} \sum_{\substack{\ell_1,\ell_2\\ \ell_3,\mathrm{m}_2}} \mathrm{m}_2\ell_2\ell_3(\ell_3+1) N_{\ell_1}^0 N_{\ell_2}^{\mathrm{m}_2} N_{\ell_3}^{-\mathrm{m}_2} \tilde{\Omega}_{\ell_1} C_{\ell_2}^{\mathrm{m}_2} C_{\ell_3}^{-\mathrm{m}_2}$$
$$\times \int_0^\pi d\theta \sin\theta P_{\ell_1}^0 P_{\ell_2}^{\mathrm{m}_2} P_{\ell_3}^{-\mathrm{m}_2}. \tag{B4}$$

Employing the identity $P_{\ell_3}^{-\mathrm{m}_2} = (-1)^{\mathrm{m}_2}(\ell_3+\mathrm{m}_2)!/(\ell_3-\mathrm{m}_2)! P_{\ell_3}^{\mathrm{m}_2}$, the integral over the product of three associated Legendre polynomials P_ℓ^m becomes a Gaunt integral of the form

$$\int_0^\pi d\theta \sin\theta P_{\ell_1}^0 P_{\ell_2}^{\mathrm{m}_2} P_{\ell_3}^{\mathrm{m}_2} = \sqrt{\frac{(2\ell_1+1)(2\ell_2+1)(2\ell_3+1)}{4\pi}}$$
$$\times \begin{pmatrix} \ell_1 & \ell_2 & \ell_3 \\ 0 & 0 & 0 \end{pmatrix} \begin{pmatrix} \ell_1 & \ell_2 & \ell_3 \\ \mathrm{m}_2 & \mathrm{m}_2 & 0 \end{pmatrix} = \begin{cases} f(\ell_1,\ell_2,\ell_3), & m_2 = 0 \\ 0, & m_2 \neq 0 \end{cases}, \tag{B5}$$

where the two parenthetical terms are Wigner 3-j symbols. The integral must be zero since $\mathrm{m}_2 + \mathrm{m}_2 \neq 0$ unless $\mathrm{m}_2 = 0$, and in the latter case the summand is zero due to the presence of the factor of m_2. Therefore, the surface terms vanish, leaving only the following volume integral

$$K_\varphi(t) = \int_V dV \Bigg[\overbrace{\overline{\rho}\lambda\langle \mathrm{v}_\varphi\rangle\langle\mathbf{v}\rangle\cdot\boldsymbol{\nabla}\langle\Omega\rangle}^{\mathrm{MC}} + \overbrace{\overline{\rho}\lambda\langle \mathrm{v}'_\varphi\mathbf{v}'\rangle\cdot\boldsymbol{\nabla}\langle\Omega\rangle}^{\mathrm{RS}}$$
$$- \overbrace{\frac{\lambda}{4\pi}\langle B_\varphi\rangle\langle\mathbf{B}\rangle\cdot\boldsymbol{\nabla}\langle\Omega\rangle}^{\mathrm{MM}} - \overbrace{\frac{\lambda}{4\pi}\langle B'_\varphi\mathbf{B}'\rangle\cdot\boldsymbol{\nabla}\langle\Omega\rangle}^{\mathrm{FM}}\Bigg]. \tag{B6}$$

Finally, it can be shown, following the derivation of the surface integral above, that the advection of the angular velocity by the meridional circulation cannot change the global kinetic energy of the differential rotation. Physically, this is a result of the fact that this mechanism simply advects energy from one part of the domain to another. Therefore, the MC term in the integral vanishes as well, leaving Equation (14) to describe the evolution of the volume-integrated kinetic energy in the differential rotation.